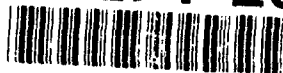


AD-A271 207



AEOSR-TR-

2

DAMAGE ACCUMULATION IN ADVANCED METAL MATRIX COMPOSITES UNDER THERMAL CYCLING/CREEP LOADINGS

M. Taya
M.S. Liu
M.L. Dunn
W.D. Armstrong
Department of Mechanical Engineering
University of Washington
Seattle, WA 98195

92-5-0369

AFOSR Technical Report (F49620-93-1-0087)
covering July 15, 1992 through July 14, 1993

September 1, 1993

DISTRIBUTION STATEMENT A
Approved for public release
Distribution Unlimited



DTIC
ELECTE
OCT 21 1993
S B D

93-25327



93 10 20 063

**DAMAGE ACCUMULATION IN ADVANCED METAL MATRIX COMPOSITES UNDER THERMAL
CYCLING/CREEP LOADINGS**

M. Taya
M.S. Liu
M.L. Dunn
W.D. Armstrong
Department of Mechanical Engineering
University of Washington
Seattle, WA 98195

AFOSR Technical Report (F49620-93-1-0087)
covering July 15, 1992 through July 14, 1993

September 1, 1993



REPORT DOCUMENTATION PAGE

1a. REPORT SECURITY CLASSIFICATION Unclassified			1b. RESTRICTIVE MARKINGS		
2a. SECURITY CLASSIFICATION AUTHORITY			3. DISTRIBUTION/AVAILABILITY OF REPORT Approved for public release, distribution unlimited		
2b. DECLASSIFICATION/DOWNGRADING SCHEDULE			5. MONITORING ORGANIZATION REPORT NUMBER(S)		
4. PERFORMING ORGANIZATION REPORT NUMBER(S)			7a. NAME OF MONITORING ORGANIZATION AFOSR		
6a. NAME OF PERFORMING ORGANIZATION University of Washington		6b. OFFICE SYMBOL (If applicable) NA		7b. ADDRESS (City, State and ZIP Code) AFOSR/NA Bolling AFB DC, 20332-6448	
6c. ADDRESS (City, State and ZIP Code) Department of Mechanical Engineering, FU-10 Seattle, WA 98195			9. PROCUREMENT INSTRUMENT IDENTIFICATION NUMBER F49620-93-1-0087		
8a. NAME OF FUNDING/SPONSORING ORGANIZATION AFOSR		8b. OFFICE SYMBOL (If applicable) NA		10. SOURCE OF FUNDING NOS.	
8c. ADDRESS (City, State and ZIP Code) Bolling Air Force Base Washington, DC 20332-6448		PROGRAM ELEMENT NO. 611007		PROJECT NO. 2302	TASK NO. B2
11. TITLE (Include Security Classification) Damage Accumulation in Advanced MMCs Under Thermal Cycling/Creep Loadings					
12. PERSONAL AUTHOR(S) M. Taya, M.S. Liu, M.L. Dunn and W.D. Armstrong					
13a. TYPE OF REPORT Annual (1st yr)		13b. TIME COVERED FROM 7/15/92 TO 7/15/93		14. DATE OF REPORT (Yr., Mo., Day) 1993, September 1	
15. PAGE COUNT					
16. SUPPLEMENTARY NOTATION					
17. COSATI CODES			18. SUBJECT TERMS (Continue on reverse if necessary and identify by block number)		
FIELD	GROUP	SUB. GR.			
19. ABSTRACT (Continue on reverse if necessary and identify by block number) Both experimental and analytical studies were conducted during the first year with the aim of identifying the damage accumulation process in a metal matrix Composite (MMC) subjected to combined creep and thermal cycling loadings. The main achievements in the experimental study are: completion of a new thermal cyler with constant stress loading capability, preliminary data of dimensional change of SiCp/6061 Al matrix composite and R-Curve behavior of PSZ-SS/PSZ composite--PSZ laminate. Whereas the first year analytical study includes construction of dislocation punching model from ceramic/metal interfaces, and construction of analytical modeling of creep strain of a MMC subjected to either creep loading or combined creep/thermal cycling loading where the debonding of the matrix-fiber interface is accounted for. Three-parameter Weibull function is employed in the model to simulate the distribution of the actual interfacial strength.					
20. DISTRIBUTION/AVAILABILITY OF ABSTRACT UNCLASSIFIED/UNLIMITED <input checked="" type="checkbox"/> SAME AS RPT. <input type="checkbox"/> DTIC USERS <input type="checkbox"/>			21. ABSTRACT SECURITY CLASSIFICATION (U)		
22a. NAME OF RESPONSIBLE INDIVIDUAL Minoru Taya			22b. TELEPHONE NUMBER (Include Area Code) 206-685-2850		22c. OFFICE SYMBOL NA

Table of Contents

	Page
1. Introduction.....	1
2. Experimental Study.....	2
2.1 Design of New Thermal Cycler with Constant Stress Loading.....	2
2.2 Preliminary Results of Dimensional Change.....	7
2.3 Fracture Toughness of PSZ-SS/PSZ-PSZ Laminate.....	8
3. Analytical Study I: Dislocation Punching from Ceramic/Metal Interfaces.....	15
3.1 Dislocation Punching from a Short Fiber.....	16
3.2 Dislocation Punching from a Spherical Particle.....	19
3.3 Dislocation Punching from a Continuous Fiber.....	22
3.4 Dislocation Punching from a Planar Interface.....	24
4. Analytical Study II: Creep and Thermal Cycling Creep of Metal Matrix Composites.....	27
4.1 Background.....	27
4.2 Analytical Model.....	28
4.3 Sample Calculations.....	36
5. Conclusion.....	39
6. References.....	40
7. List of Publications During the First Year Period.....	42

Accession For	
NTIS GRA&I	<input checked="checked" type="checkbox"/>
DTIC TAB	<input type="checkbox"/>
Unannounced	<input type="checkbox"/>
Justification	
By	
Distribution/	
Availability Codes	
Dist	Avail and/or Special
A-1	

DTIC QUALITY INSPECTED 2

I. Introduction

One of the most severe use conditions for advanced metal matrix composites (MMCs) is combined creep and thermal cycling loadings. For dimensional change of the MMC subjected to combined creep and thermal cycling is presumably much larger than those under either creep loading or thermal cycling (Wu and Sherby, 1984; Wakashima et al., 1986; Pickard and Derby, 1989, Le Flour and Locicero, 1990). Wu and Sherby (1984) observed that the creep rate ($\dot{\epsilon}_c$) of 20% V₁SiCw/2024 Al composite under thermal cycling is much larger than the creep rate of the composite without thermal cycling for the same constant applied stress (σ_c) as shown in Fig. 1.1. The conditions of the creep/thermal cycling testing of Wu and Sherby are that $T_{max} = 450^\circ\text{C}$, $T_{min} = 100^\circ\text{C}$, and the creep loading is compression. It is also seen from Fig. 1.1 that the stress exponent, n , in the isothermal case (creep loading only) is constant over the stress range studied and equal to 20, while that in the case of creep over the stress range studied with thermal cycling loading is much smaller (of order 1) and is a function of stress. This large dimensional change observed in an MMC subjected to creep/thermal cycling loading is termed superplasticity by Wu and Sherby, and it is apparently caused by the internal stress field with reverse loadings during the thermal cycling. This internal stress is believed to be induced by the CTE mismatch strain discussed earlier.

During the first year, we conducted both experimental and analytical studies; the former includes construction of new thermal cycler with capability of constant stress, documentation of dimensional change of SiC particulate/6061 Al composite and evaluation of the fracture toughness of layered ceramic/metal composite, while the latter is aimed at construction of an analytical model to predict the dimensional change of a MMC subjected to constant stress and thermal cycling where the effect of interfacial bonding was examined. We have conducted additional analytical work to construct a dislocation punching model for various types of interface. In the following two chapters, the results of the above experimental and analytical studies will be stated.

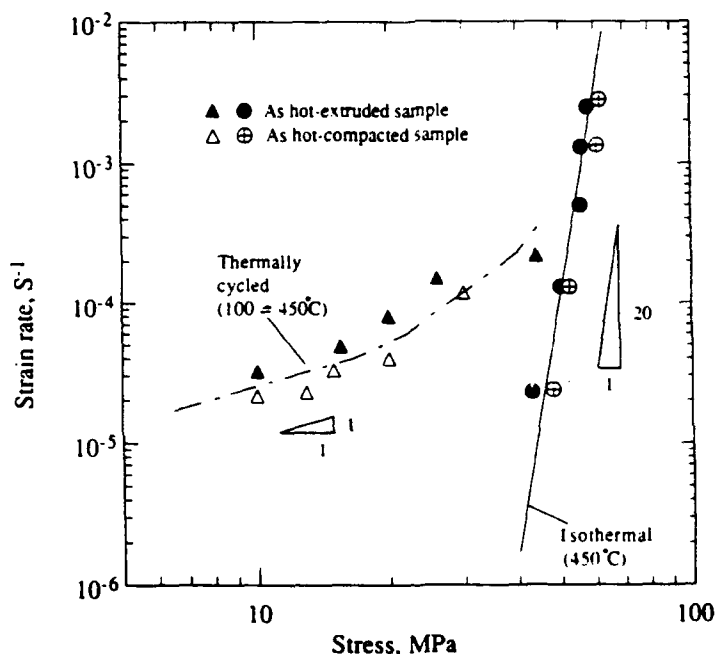


Fig. 1.1 Strain-rate vs. applied stress of SiCw/2024 Al composite under constant stress with and without thermal cycling (Wu and Sherby, 1984).

2. Experimental Study

The major effort in the experimental study has been devoted to construction of a new thermal cycler with constant stress loading and to obtain preliminary data of dimensional change of SiC particulate/6061 Al composite subjected to both thermal cycling and constant stress. We also studied the fracture behavior of a new class of metal matrix composite, layered metal/ceramic composite.

2.1 Design of New Thermal Cycler with Constant Stress Loading

In order to cover both low temperature metal matrix composite (SiC/Al) and high temperature metal matrix composite (W/FeCrAlY), the system was designed to apply temperature fluctuation up to 1400° C while it is subjected to a constant stress up to 150 MPa. In order to control the specimen temperature accurately, the specimen is loaded under constant stress stationary while constant temperature furnaces are moving. The furnaces are shuttled from one station to the other with a 1/4 horsepower 12 V DC electric motor driven wire cables. The station hold time can be set independently for each furnace in 30 second increments up to a maximum of seven and a half minutes. Additionally the adoption of constant temperature furnaces increased the expected reliability of the system by avoiding the furnace degradation processes due to thermal cycling of the furnace itself. Because of this the system is expected to provide reliable thermal cycle tests of 10,000 cycles duration. The test stand is designed to apply static stress to a test specimen for an extended period of time under a constant elevated temperature or cycling temperature. The test stand consists of a balancing cam and a constant-load wheel that connects the test specimen to a weight pan, as shown in Fig. 2.1. Ratio of 4.05 is used between the weight pan and the specimen. The weight pan is a part of the overall weights and is suspended with a chain to prevent bending moments on the load train. The load frame can be divided into two main part sets; front frame and rear frame. The front frame is primarily constructed of 10.2 cm high by 5.2 cm wide by 6.35 mm wall thickness A500 grade steel rectangular tube, while the rear frame of L2.5x2.5x1/4 steel angles.

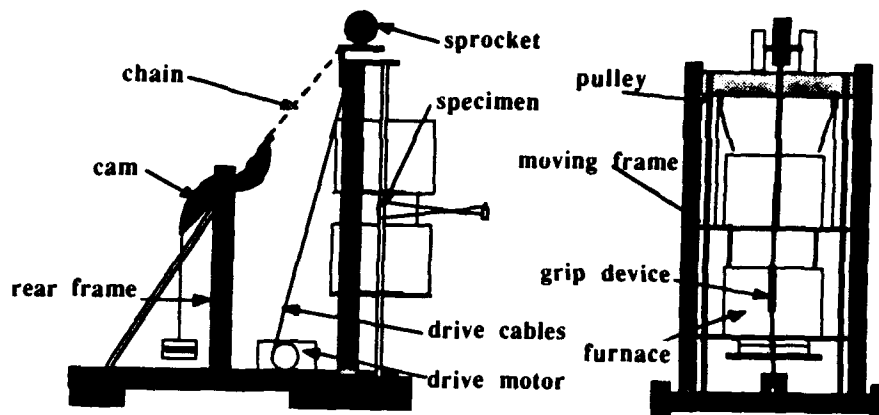


Fig. 2.1 New thermal cycler with constant stress loading.

Design for constant-stress condition

Creep and thermal fatigue data are usually obtained under constant-load test conditions. It is often desirable and necessary to obtain test data under constant -stress condition in the case of large strains. In this case, the applied load is adjusted as the length of the specimen changes to maintain constant stress on the specimen. A compact cam-lever apparatus for application of either constant stress or constant load in tension for large uniform deformations has been used (Fig. 2.2). The load to the specimen is applied through a circular disk of radius R (Fig. 2.2). The initial load magnification factor is r_0/R , but the factor is reduced as the specimen elongates. To maintain constant stress, the load P on the specimen must be reduced as the specimen elongates to compensate for the reduction in area A . Thus, the instantaneous stress P/A must remain constant. By assuming constant specimen volume and uniform strain, LA (where L is the specimen gage length) must remain constant. Therefore, it follows that PL also remains constant. In Fig. 2.2, under equilibrium conditions, $P=Wr/R$, where W is the applied weight and r is the instantaneous moment arm of the applied weight.

Thus, to maintain a constant stress, the following condition must be satisfied:

$$rL = \text{constant} - r_0L_0 \quad (2.1)$$

where L_0 is the initial specimen length, and r_0 is the initial value of r .

Thus the equation of the profile of a constant-stress cam is obtained as follows:.

$$L = r_0L_0 / (L_0 + (\Theta - \Theta_0)) \quad (2.2)$$

where Θ_0 is the angle for the initial positioning of the constant-stress cam, and it can be easily transformed into a fixed Cartesian coordinate system (x,y) (Garofalo et al, 1962).

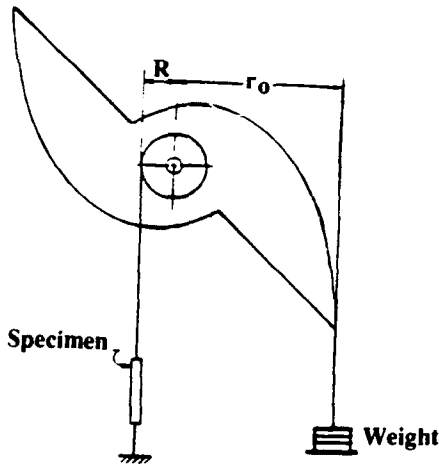


Fig. 2.2 Cam-lever system.

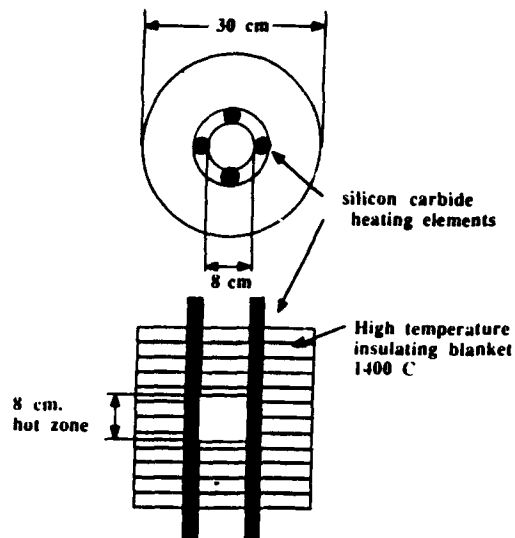


Fig. 2.3 Schematic of moving furnace.

To provide balance and proper control of loading on the specimen, a balancing is added to the loading cam. A circular disk or constant-load wheel also designed and can replace the cam for the purpose of performing constant-load testing. The load is transmitted by DIAMOND 40SS stainless steel roller chain which may be used in ambient temperature up to 300° C. The actual use temperature on it is 100° C. The shaft of the cam assembly is supported by pillow block bearings.

The machine is equipped with two 30 cm high by 30 cm in diameter resistance element furnaces as shown in Fig. 2.3. The furnaces are mounted on a moving frame which slides on guides attached to the reaction frame. The furnaces are powered by four 35.6 cm long by 2.54 cm diameter silicon carbide heating elements. Each heating element has a 10.2 cm hot section. The maximum steady operating temperature of the furnaces is 1400°C. At a typical maximum cycle temperature of 1100°C the steady state operating power requirement is 5000 watts. When silicon carbide heating elements are heated in air, an oxidation process begins that will slowly increase the resistance of the bar. Initially the oxidation process is slow, but the oxidation rate continues to climb at an ever-increasing rate.

The furnaces are controlled to a set temperature by a Barber Coleman 560 controller and a phase SCR (Silicon Controlled Rectifier) power switch, shown in Fig. 2.4. SCR power switch differs from other switches in its fast action. For example, while a controller may cycle three times per minute, SCR cycles approximately once per second. This fast SCR cycle time result in process temperature maintenance much closer to the desired set point. The SCR modulates small increments of power to the load, unlike traditional mechanical control, and eliminates the overshoot and undershoot associated with contactor control. In this design, the type R thermocouple is used for the controllers. Ordinarily the controllers are powered by the same current as the furnaces. In our case the low resistance of the element circuit required a low voltage high amperage furnace current while the controller logic circuit required the original 240 volt input current.

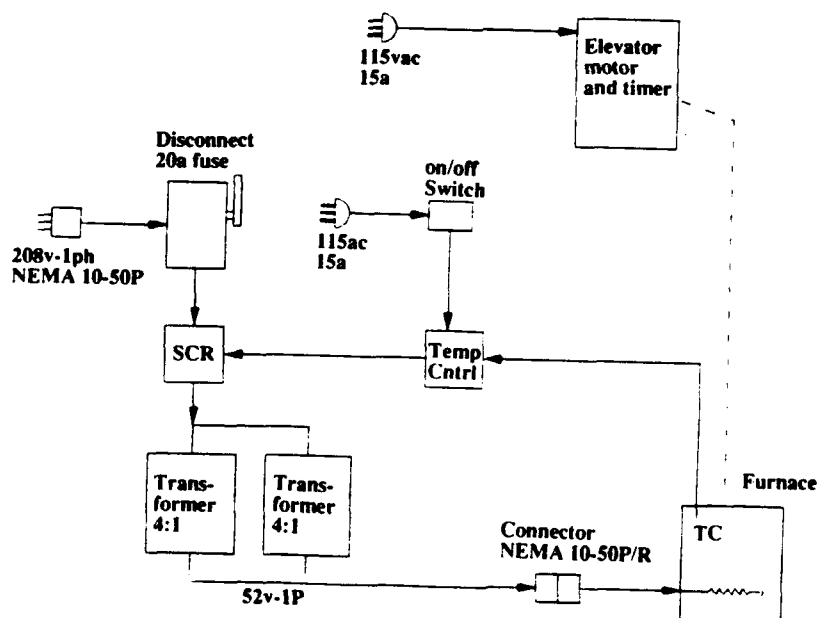


Fig. 2.4 Wiring of the thermal cycler.

Furnace Transport System

The furnace transport control system can be conveniently divided into a furnace cycle controller and a motor relay. The motor relay supplies the drive motor with the appropriate polarity of 12 V DC current when triggered by the cycle controller. The direct current is supplied by an automotive battery which is charged with a 1.5 amp trickle charger. The furnace cycle controller directs the furnace motor relay. The furnace cycle controller contains two four-bit switches which are used to preset a counter at the completion of a furnace transport event. This counter reduces its total count by one when signaled by a clock circuit. When the counter has been counted back to zero the motor relay is directed to supply current to the drive motor.

Position switches mounted on the furnace guide rods set the furnace cycle controller logic so as to direct the motor relay to provide current of the correct polarity. The furnace cycle controller system is equipped with three limit switches which can disable the motor circuit. Two of these switches are mounted on the furnace guide rods beyond the position switches. These switches are to ensure that the motor will not drive the furnaces up into the loading lever or lower them onto the reaction lever. The third disable switch is placed on the loading lever support to stop any furnace transport in the event of a specimen or load train failure.

Load Train

The load train is a set of parts which connect the loading lever and the reaction lever to the specimen. The load train must sustain a large tensile load while being subjected to the time-temperature conditions imposed by the moving furnaces.

The load train is composed of chain with sprocket, one coupler, two long bars, two inconel grips, and a test specimen (see Fig. 2.1). The chain is made of stainless steel. The actual temperature on the chain is only about 100°C. The chain connects one side of tensile bar with the sprocket in the rear shaft to convey load from the rear frame to the front frame. The load train coupler is made of mild steel. The coupler has a one inch horizontal hole through which runs a hardened steel pin. The coupler has also drilled and tapped to mate vertically with the threaded stainless steel rods. The steel rods connect with high temperature inconel grips which are drilled and tapped to mate with the test specimen (see Fig. 2.1 and Fig. 2.6).

Temperature-Time Curve

Figure 6 shows an example of temperature-time curves plots measured with a thermocouple which is located on the surface of aluminum specimen. All the data sets used forced air convection to cool the specimen. The data were measured for nine and half a minute cycle where the maximum temperature (T_{max}) was 200° C, 250° C, and 300° C respectively.

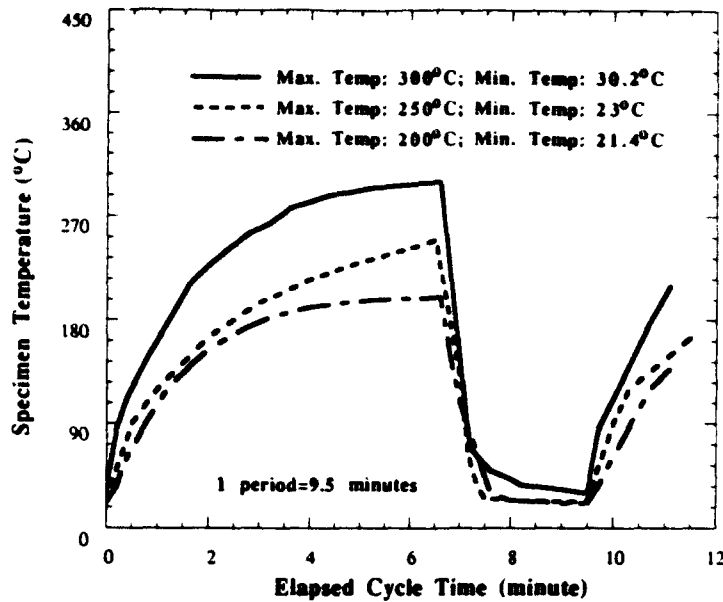


Fig. 2.5 Typical temperature-time curves for $T_{\max} = 200, 250, \text{ and } 300^{\circ}\text{C}$.

Specimen Preparation and Loading

In this research, a specimen with shouldered ends "buttonhead" (no threads) is used for tests conducted at very high temperatures, as shown in Fig. 2.6(a). Buttonhead specimens and adapters, as shown in Fig. 2.6(b), tend to be self-aligning and pose fewer alignment problems. The material of the Adapters are Inconel 600 which has high oxidation resistance up to about 1400°C . Meanwhile, the stress in the grip bar is only about one eleventh of that in the specimen because the ratio square of the cross section of the grip bar over that of the specimen is 11:1. Similarly, the maximum stress in the adapter is only about one fifth of that in the specimen. So, the stress level in both the adapter and the grip bar is much smaller than that in the specimen, and their degradation is expected to be much smaller. Care is required to avoid straining the specimen when mounting it in the adapters and load train. With the specimen in place, the load train (specimen adapters or grips, pull rods, etc.) is examined carefully for any misalignment that may cause bending of the specimen under load. The specimen is stabilized at temperature before loading. Loading the weight pan is done smoothly and without excessive shock. This can be done by placing a support, a scissors jack under the load pan during loading. When all weights are in place, the supporting jack is lowered smoothly from under the weight pan.

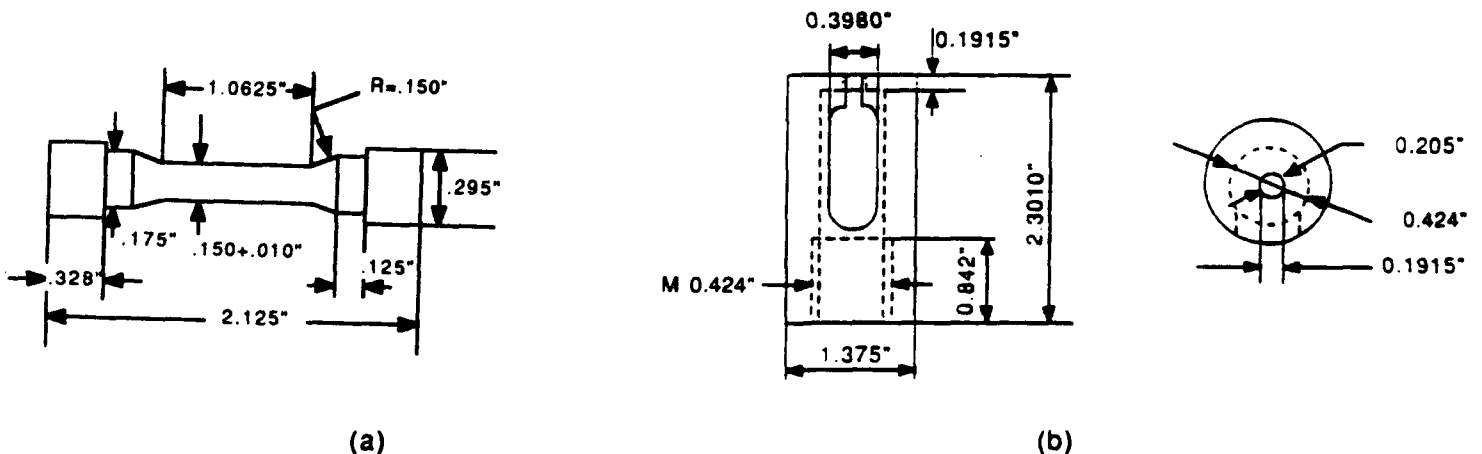


Fig. 2.6 Dimensions of a specimen (a) and its grip device (b)

2.2 Preliminary Results of Dimensional Change

By using the new thermal cycler with constants stress (σ) loading capability, we conducted testing on SiC particulate/6061 Al (SiCp/Al) composite. With two different volume fractions of particulate $V_f = 10\%$ and 20% . The testing conditions are $T_{min} =$ room temperature, $T_{max} = 300$ and 350°C , $\sigma = 18.1$ and 24.6 MPa. The results of axial dimensional change of SiCp/Al composite are plotted as a function of number of thermal cycles (N) in Fig. 2.7. The dimensional change- N relation of SiCp/Al composite subjected to thermal cycling and constant stress exhibits initially linear, but tends to be flattened for larger N 's. This is in marked contrast with that of W fiber/Cu (Yoda et al., 1978) and W fiber/superalloy matrix composite (Taya et al., 1991) which are subjected to thermal cycling only, where the dimensional change increases with N linearly for smaller N 's but the rate of increase increases with N , as schematically shown in Fig. 2.8. Sharp increase on the slope of dimensional change- N relation for larger N 's is attributed to debonding of the matrix-fiber interface as will be discussed later. The dimensional change- N relation observed in SiCp/Al composite in this study implies that the bonding of the SiC particulate-Al matrix interface is strong. If the bonding were not, the dimensional change would have been enhanced as N increases like Fig. 2.8.

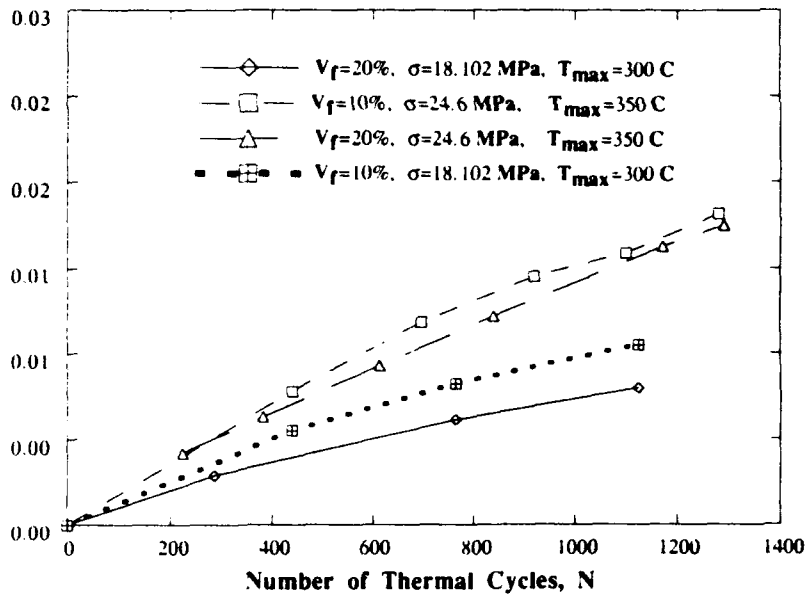


Fig. 2.7 Dimensional change- N relation of SiCp/6061 Al composites subjected to thermal cycling and constant stress.

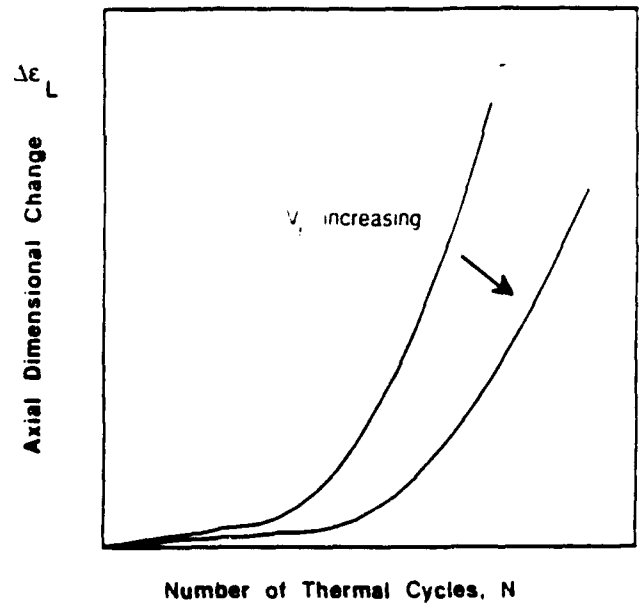


Fig. 2.8 Schematic of dimensional change- N relation of W/Cu and W/superalloy composites subjected to thermal cycling only.

It is seen from Fig. 2.7 that an increase in volume fraction of particulate (V_f) is to decrease dimensional change which is confirmed analytically for the case of short and long fiber MMC (Taya et al., 1991), Fig. 2.8, although the analytical study for the case of a particle MMC has not been made yet, hence the prediction of the dimensional change would not be available. Fig. 2.7 also indicates that an increase in applied (constant) stress σ increases the dimensional change, which has been confirmed by Pickard and Derby (1990). This has also been confirmed by our recent analytical study which was developed for a short fiber MMC (Dunn and Taya, 1992). Testing on SiCp/Al composite specimens under other conditions, $T_{max} = 250^\circ\text{C}$, $\sigma = 30 \text{ MPa}$ remains to be done. Also the evaluation of the residual mechanical properties of as-tested composites needs to be conducted.

2.3 Fracture Toughness of PSZ-SS/PSZ Composite-PSZ Laminate

Ceramics has not only high stiffness, high compressive strength and high hardness, but also good fatigue resistance, good creep and corrosion resistance. These material properties make ceramics very useful in engines, cutting tools and some structure designs in aerospace engineering. Despite the above advantages, the toughness or crack growth resistance of ceramics is low, typically $2\text{--}5 \text{ MPa}\sqrt{\text{m}}$. This disadvantage really weakens the load carrying capacity of a ceramic structure and impedes the wide application of this material. One of the methods to improve the fracture toughness is to reinforce the ceramics with fillers (fibers and particles) and form a ceramic matrix composite (CMC). The microstructure in a CMC is normally homogeneous, i.e. the volume fraction of fillers is uniform spatially. It would be interesting to examine the fracture toughness as a function of crack extension (so called R-curve) of CMC if the microstructure of the CMC is not uniform. An example of such a CMC with non-homogeneous microstructure is shown in Fig. 2.9 where pure ceramic (partially stabilized zirconia, PSZ in short) sandwiches stainless steel/ PSZ composite (ceramic matrix composite, SS/PSZ composite in short). It would be valuable to assess the effect of the SS/PSZ composite layer on the R-curve behavior of the laminate which is expected to exhibit a transition behavior at the PSZ ceramic-SS/ PSZ composite interface as schematically indicated in Fig. 2.9. The purpose of this study is to assess the R-curve behavior of the PSZ-SS/PSZ composite-PSZ laminate composite experimentally.

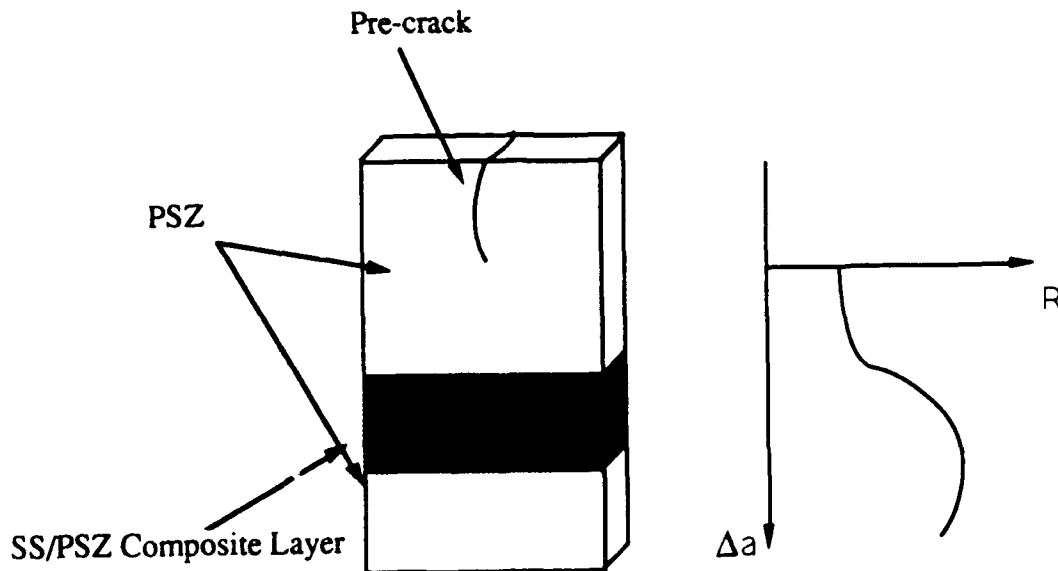
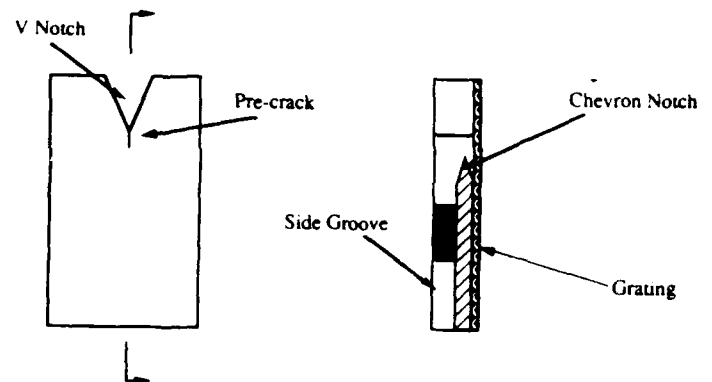
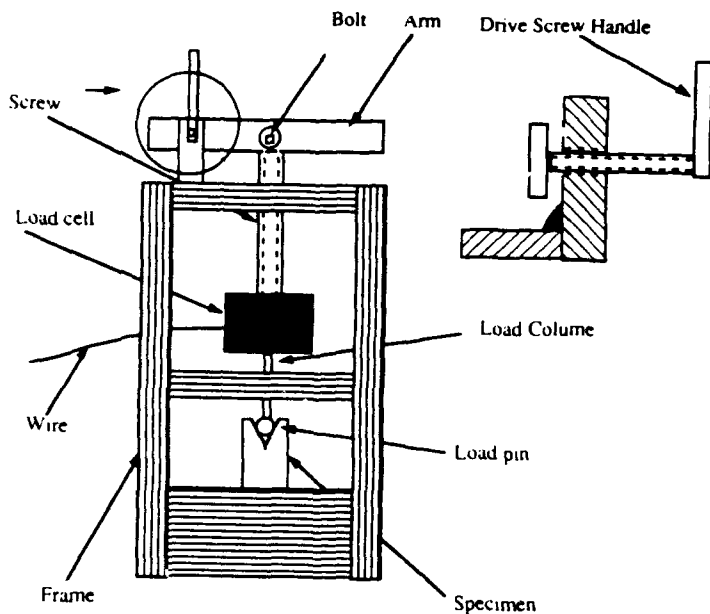


Fig. 2.9 PSZ-SS/PSZ composite-PSZ laminate and expected R-curve

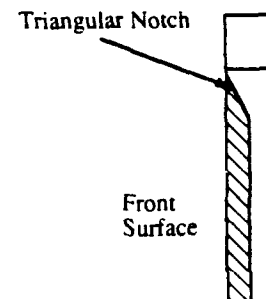
2.3.1 Experiment

Loading Device and WL-DCB Specimen

The loading device shown in Fig. 2.10 can load or unload a specimen respectively by clock-wise or counter clock-wise turn of the arm which is sensitively controlled by turning of the drive screw handle. The load is determined by the strain in the load cell which is connected with the strain gage indicator—model 3270, whose output numbers in the display are linearly related to the virtual load (P) on the specimen. Unlike some other loading device in which the load is controlled by weight, this load is controlled by the displacement at the load point between loading pin and surface of the specimen. When the load increases, the displacement is increased, in the meantime, the increased displacement will reduce the load a little. This device is called displacement controlled loading device, or COD-feedback loading device, since this displacement is related to crack opening displacement (COD). In order to control the speed of crack propagation, wedge-loaded double cantilever beam (WL-DCB) specimen with Chevron notch is selected (Fig. 2.11(a)). The cutting process is accomplished by using the diamond blade in the machine LEEMATIC 2000 surface grinders/slices. Some improvements are made in the geometry and dimension of the specimen. The Chevron notch is replaced by the triangular notch (Fig. 2.11(b)), the V notch angle is reduced from 60° to 45° and the width of the specimen is cut significantly into a narrow one. By doing so, one can obtain a pre-crack more easily.



(a)



(b)

Fig. 2.10 Loading device and WL-DCB specimen

Fig. 2.11 WL-DCB specimen: (a) chevron notch, (b) triangular notch.

Moiré Interferential Optical System

In order to measure the fracture toughness, one can use data of COD of a specimen and the results of finite element analysis (hybrid-experimental-numerical method). Moiré interferential is a reliable displacement measurement method which can measure COD of the specimen used in this experiment. The details of the principle of the Moiré interferometry can be found elsewhere (Post, 1987). Moiré interference can be produced by several different optical systems. The main part of the work is to obtain two coherent parallel lights from the right angle. In this experiment, a simple optical set-up as shown in Fig. 2.12 is used, where the second beam of coherent light is obtained with assistance of mirror 2 instead of two laser radiators. The function of the special filter and lens is to get a disk of parallel light, which should cover Mirror 2 and the specimen. The red laser beam comes from the Model 159 10mw Helium-Neon laser generator. Due to low power, there is no fan in the radiator. This is very important, because if the vibration is brought from the fan, it will affect the fringes. In this experiment, the grating frequency is 1200 lines per millimeter, and the wavelength of the He-Ne red laser light is 6328nm which is equal to $6328 \times 10^{-10} \text{m}$, hence the angle of the incident light is given by

$$\alpha = \sin^{-1} \frac{f\lambda}{2} = \sin^{-1} \frac{1200 \times 6328 \times 10^{-7}}{2} = 22.3^\circ \quad (2.3)$$

Since the fringe pattern directly represents the displacement field, it is used to measure CODs which are in turn used to compute elastic energy. Following the principle of the moiré fringe in deformed field, the x-direction displacement (u) can be found in the fringe pattern, and given by

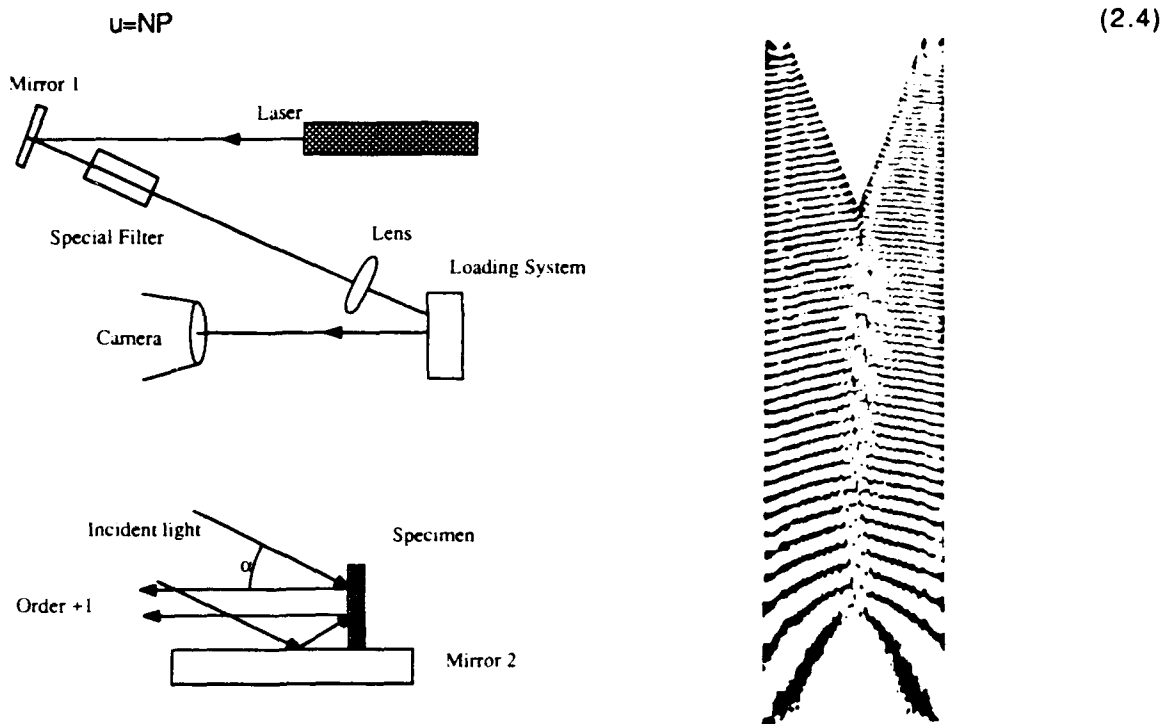


Fig. 2.12 Moiré interferometry system for displacement measurement.

Fig. 2.13 An example of Moiré pattern.

Where N is fringe order and P is pitch of the grating. There exists a difference between geometry Moiré and Moiré interferometry. In the Moiré interferometry, the pitch of the grating must be used as half of the real pitch. For example, if the pitch of the grating (P) is 1/1200 millimeter, when the displacement is calculated by eq. (2.2), the effective pitch (P_{eff}) should be 1/2400 millimeter. Fig. 2.13 is one of the moiré fringe patterns observed in this experiment.

Basically, the zero-order fringe, which has no x-direction displacement on the fringe, is a bright straight line at the specimen's symmetric center connected with the crack tip. Next to the zero-order fringe is the dark half-order fringe, which represents displacement of the half pitch of the effective grating.

$$u = NP_{eff} = N \frac{P_{real}}{2} \times \frac{1}{2400} = 0.2083 \times 10^{-3} \text{ (mm)} \quad (2.5)$$

Similarly, the fringe order at load point can be counted, for example for $N = 56.5$, the displacement is

$$u = NP_{eff} = 56.5 \times \frac{1}{2400} = 23.542 \times 10^{-3} \text{ (mm)} \quad (2.6)$$

Since the load and geometry of the specimen are symmetrical, only a half of the specimen is used to compute the R-curve. However in reality, due to the error of the grating coating, the fringe pattern is often not symmetrical. Thus the average number is used to represent x-displacement.

Experimental Procedure

First, one must adjust the angle of the mirror 2 in Fig. 2.12 to obtain horizontal parallel fringe lines when the load is zero. The fewer these lines, the more accurate the optical system is adjusted. With the increase of the load, both the numbers of the fringes and the shape of the fringes are changed. In order to keep the fringe pattern symmetrical in this procedure, the angle of mirror 2 must be adjusted every time when an increase of load is applied. But only one direction of the angle needs to be adjusted, either up and down or left and right; otherwise, CODs of the specimen are not accurately shown by the fringe pattern. In fact, the absolute symmetric fringe pattern is very hard to maintain during the experiment, so the CODs measured at both edges are averaged.

Without a successive stable crack growth, the R-curve can not be obtained. Thus the load must be increased very slowly.

Computation of Energy Release Rate

Energy release rate is defined by

$$G = \frac{d(F-U)}{da} \quad (2.7)$$

where F is work done by external force, U is elastic energy contained in the specimen and a is the crack length. In the actual computation, the derivative in the eq. (2.8) is approximated by the incremental form:

$$G_n = \frac{\Delta F - \Delta U}{\Delta a} = \frac{(F_{n+1} - F_n) - (U_{n+1} - U_n)}{(a_{n+1} - a_n)} \quad (2.8)$$

This requires the experimental procedure of continually recording the load, crack length and displacement from which the R-curve is computed.

Since PSZ and PSZ/SS composite are both brittle material, only elastic energy is considered in this case, and the analysis and computation can be based on linear elastic fracture mechanics (LEFM). In this fracture test, load in y direction is read by the strain gage indicator while the displacement in x direction at loading point by the Moiré fringe pattern

External work and elastic energy can be computed by a finite element method (FEM). For a crack extension Δa in the specimen, a new mesh is generated and new external work and elastic energy are computed. Then by the use of eq. (2.5), the energy release rate is computed. The contribution to the energy change by Y component of the force (F_y) is so small, thus it can be neglected compared with the contribution by the displacement in x-direction. Then the eq. (2.5) can be simplified as

$$G_n = \frac{U_n - U_{n+1}}{a_{n+1} - a_n} = R_n \quad (2.9)$$

In this equation, a_{n+1} is always larger than a_n and U_{n+1} is always less than U_n , hence the R_n is always positive.

Due to the symmetry of the specimen geometry and the load, only a half of the specimen geometry needs to be considered. Along the crack growth line, the denser mesh is needed and the node position around the crack tip should be changed to the quarter node. By doing so, a more accurate computation result can be achieved.

2.3.2 Result and Discussion

R-curve of PSZ-SS/PSZ Composite-PSZ Laminate

The experiment is performed on three specimens: one specimen made of PSZ only and two PSZ-SS/PSZ composite-PSZ laminate specimens with two different volume fraction of SS in the SS/PSZ composite area. The dimensions of the specimens are identical and they are shown in Fig. 2.14.

The mechanical properties of SS, PSZ and SS/PSZ composite are shown in Table 2.1, where those of the composite are estimated by using the Eshelby's model (Taya and Arsenault, 1989).

In order to examine the effects of SS phase on the R-curve behavior in PSZ-SS/PSZ composite-PSZ laminate, two specimens are used: one contains 10% SS, another one 20% SS in SS/PSZ composite layer. As a reference, a pure PSZ specimen is also used. The results of R-curve (energy release rate) of these three specimen as a function of Δa are shown in Fig. 2.15, where SS/PSZ composite layer (CMC) region is indicated by horizontal bar.

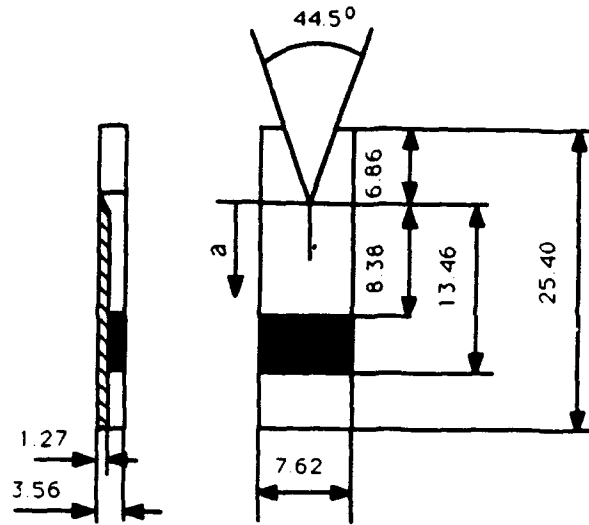


Fig. 2.14 Dimensions of PSZ-SS/PSZ-PSZ laminate specimen.

Table 2.1 Mechanical Properties

	E (GPa)	Poisson's rate ν	CTE ($10^{-6}/C^{\circ}$)
SS	196	0.26	14.0
PSZ	168.8	0.3	11.1
10%SS+90%PSZ	171.4	0.296	11.3
20%SS+80%PSZ	174.0	0.292	11.6

It is often useful to convert R-curve to K_R - Δa relation, where K_R is the critical stress intensity factor or fracture toughness at a given crack length Δa . In plane stress condition

$$K_R = \sqrt{ER} \quad (2.10)$$

where E is modulus of elasticity and R is crack growth resistance. Note in this formula, different values of E should be used in the different region. Fig. 2.16 is the K_R - Δa relation obtained from Fig. 2.15 and eq. (2.10).

It is clear from Figs. 2.15 and 2.16 that the energy release rate (R) and fracture toughness (K_R) which are small during early stage of crack propagation, jump to a relatively large value once the crack advances the CMC region. The jump in terms of K_R is almost twice as large as that of unreinforced PSZ specimen. Figs. 2.15 and 2.16 also show the gradual increase in R- Δa or K_R - Δa curve in early stage of crack propagation characteristics with brittle materials.

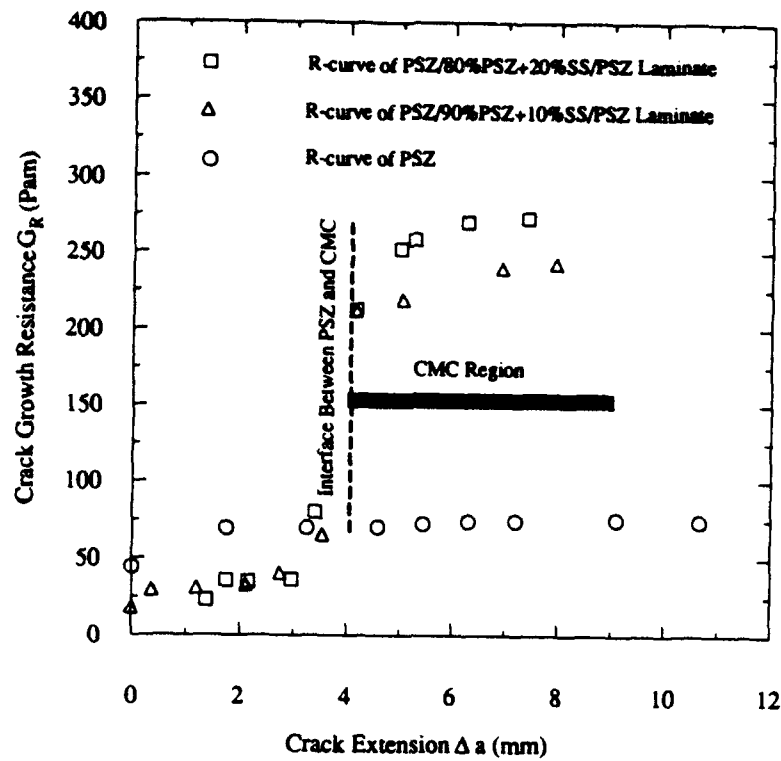


Fig. 2.15 $R(G_R) - \Delta a$ relation.

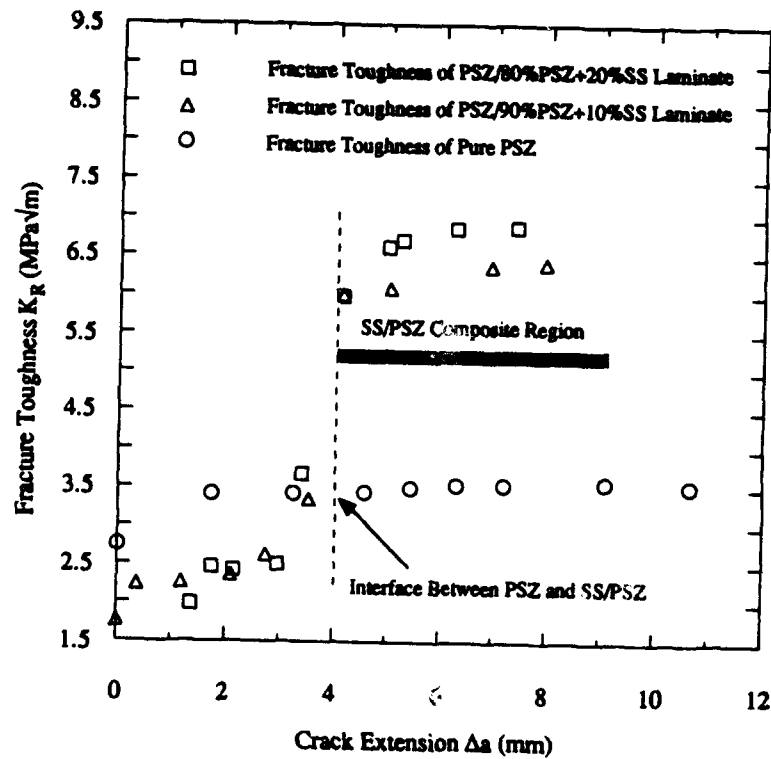


Fig. 2.16 $K_R - \Delta a$ relation.

3. Analytical Study - I: Dislocation Punching From Ceramic/Metal Interfaces

When two different materials are bonded, misfit strain exists at the interface at and around which high stress field is induced. This misfit strain at the interface is due to the mismatch in the stiffness of the materials and in coefficient of thermal expansion (CTE) under temperature change. The order of the misfit strain due to CTE mismatch can be quite large for larger temperature changes. Microscopically this misfit strain at the interface is accommodated by dislocations near the interface. When the magnitude of the stress field becomes too large, relaxation of the stress of large magnitude is more likely to take place. Punching of dislocations from the interface is such a relaxation mechanism and has been observed in dispersion-hardened alloys (Hedyes and Mitchell, 1953; Weatherly, 1968; Ashby and Johnson, 1969), metal matrix composites (Chawla and Metzger, 1972; Vogelsang et al., 1986; Taya et al., 1991), and metal coating/ceramic substrate system (Shieu and Sass, 1990).

The dislocation punching model was first used by Ashby (1966) to explain the strengthening mechanism of dispersion-hardened alloys subjected to shear (plastic) strain γ where the punching of prismatic dislocation loops along the secondary slip planes is assumed. The work-hardening predicted by the Ashby's model is

$$\tau - \tau_y = 0.24\mu\sqrt{bf\gamma/d} \quad (3.1)$$

where τ and τ_y are the flow stress and initial yield stress in shear, μ , b and γ are the shear modulus, the Burgers' vector and plastic shear strain of the matrix, respectively, and f and d are the volume fraction and diameter of particles. The Ashby's model predicts well the parabolic dependence of τ on γ observed in the experiment. The misfit strain in the Ashby's model before punching is represented by arrays of edge dislocations piled up at the particle/matrix interface. Tanaka and Mori (1970) solved the problem of misfit strain at the interface by using the Eshelby's model (Eshelby, 1957) where the misfit (plastic) strain at the particle/matrix interface is smeared out to become "transformation strain" (Eshelby, 1957) or "eigenstrain" (Mura, 1987). The stress-strain relation of a composite predicted by the Tanaka-Mori model is given by

$$\sigma_o = \sigma_y + h e_p \quad (3.2)$$

where σ_o and σ_y are the flow stress and initial yield stress, h and e_p are the work-hardening rate and plastic strain along the loading direction. The linear relationship between $\sigma_o - \sigma_y$ (work-hardening) and plastic strain e_p in the above equation agrees with the experiment for small range of plastic straining. For larger plastic straining, however, stress-strain curve deviates from the linear work-hardening predicted by the Tanaka Mori model. Tanaka et al. (1972) proposed a model to account for non-linear work-hardening at larger strains by using a dislocation punching model.

Modeling of dislocation punching in a metal matrix composite subjected to temperature change ΔT was first studied by Arsenault and Shi (1986) who used an equiaxed particulate (its length t) as a reinforcement and obtained the average dislocation density in the matrix metal, $\bar{\rho}$ given by

$$\bar{\rho} = \frac{12fe_T}{b(1-f)} \frac{1}{t} \quad (3.3)$$

where f is the volume fraction of particulates, e_T is CTE mismatch strain ($\Delta T \Delta \alpha$), b is Burgers' Vector. Once $\bar{\rho}$ is calculated, the increase in the matrix flow stress due to CTE mismatch strain, $\Delta \sigma_{CTE}$ may be estimated by

$$\Delta \sigma_{CTE} = \beta b \mu \sqrt{\bar{\rho}} \quad (3.4)$$

where β is a constant of order 1, μ is the matrix shear modulus.

Since 1986, more rigorous dislocation punching models have been developed by Taya and his co-workers, and they are aimed at various types of reinforcement geometry: spherical particle, short fiber, disc-shaped filler and continuous fiber. In this paper, we shall review recent studies on dislocation punching models for these types of reinforcement, and also the dislocation punching model for thin film/substrate system.

3.1. Dislocation Punching From a Short Fiber.

Taya and Mori (1987) studied analytically the dislocation punching from a short fiber in a short fiber metal matrix composite (MMC). A short fiber is simulated by a prolate ellipsoidal inhomogeneity to make use of the Eshelby's method and the CTE mismatch strain e_T is initially adhered to the fiber-matrix interface as surface dislocations (prismatic dislocation loops), Fig. 3.1(a). Due to the fact that the stress at fiber-ends is highest and the punching of the dislocation loops are favorable along the fiber axis (x_3 -axis), some of the dislocation loops are punched along the x_3 -axis, Fig. 3.1(b).

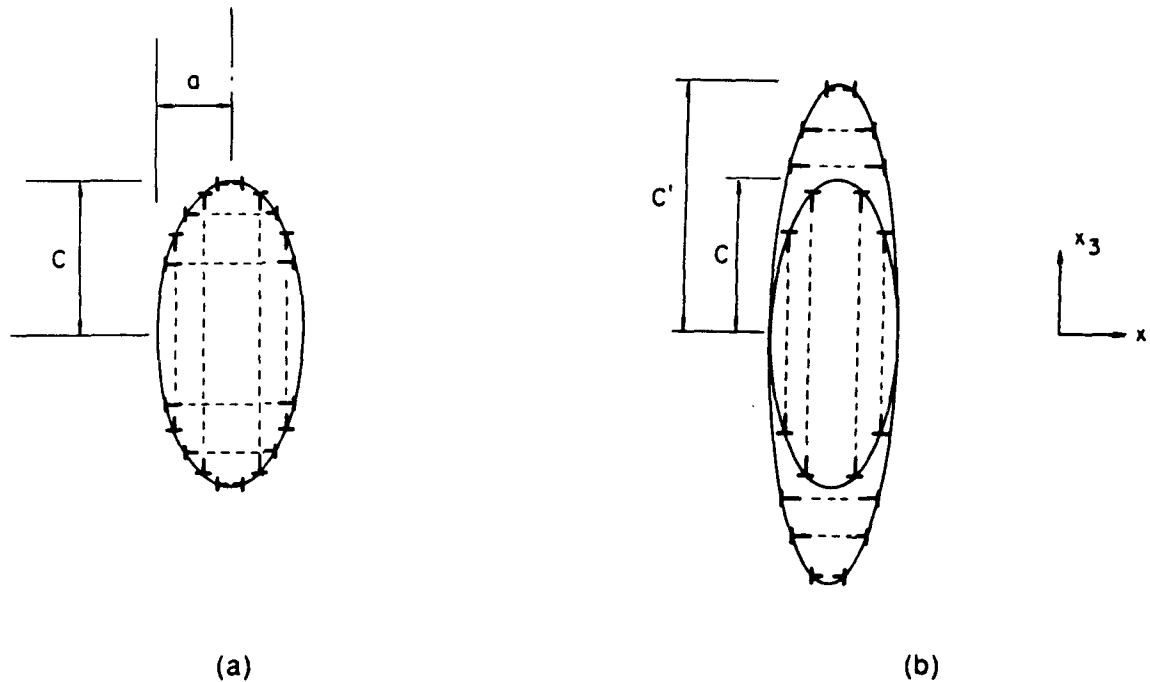


Fig. 3.1 Analytical model used by Taya and Mori (1987) to study the relaxation of CTE mismatch strain at short fiber/metal matrix interface by dislocation punching: (a) before punching (unrelaxed stage), (b) after punching (relaxed stage)

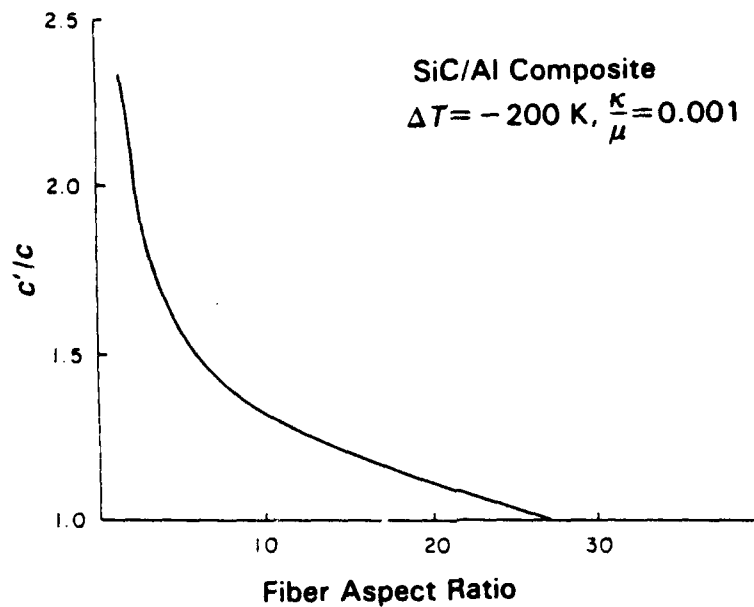


Fig. 3.2 Punching distance (c') normalized by half of short fiber length vs. fiber aspect ratio (c/a) for SiC short fiber/Al matrix composite with $\Delta T = -200^\circ\text{C}$, $\kappa/\mu = 0.001$.

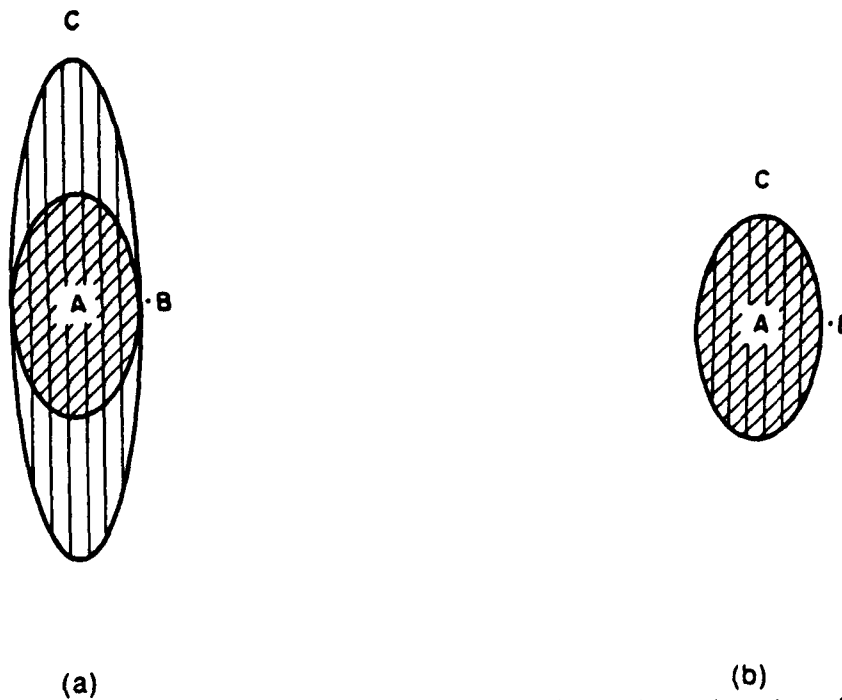


Fig. 3.3 Stresses are calculated at points A, B, and C for (a) relaxed and (b) unrelaxed stages.

The stress field in and around a short fiber and the total strain energy of a short fiber MMC can be calculated if the following eigenstrains are given in the domains of fiber (Ω_1) and of the punched region encompassing the fiber (Ω_2):

$$\tilde{e}^{*1} = \begin{Bmatrix} e_T & 0 & 0 \\ 0 & e_T & 0 \\ 0 & 0 & 0 \end{Bmatrix} \text{ in } \Omega_1 \quad (3.5)$$

$$\tilde{e}^{*2} = \begin{Bmatrix} 0 & 0 & 0 \\ 0 & 0 & 0 \\ 0 & 0 & e_T \left(\frac{c}{c'} \right) \end{Bmatrix} \text{ in } \Omega_2 \quad (3.6)$$

where c' and c are the punching distance and half of short fiber length along the x_3 -axis, respectively, Fig. 3.1. The criterion for dislocation punching is given by

$$-\frac{\partial U}{\partial c'} = \frac{\partial W}{\partial c'} \quad (3.7)$$

where U is the total strain energy of the composite of Fig. 3.1(b) and its explicit expression is given elsewhere (Taya and Mori, 1987), and W is the total energy dissipation due to punching, i.e., plastic work required for the motion of the dislocation loops during punching and given by

$$W = \left(\frac{c}{a} \right) f k \left(\frac{c'}{c} - 1 \right) e_T \quad (3.8)$$

where c/a is the fiber aspect ratio, k is the friction stress of the matrix metal against dislocation motion.

Equation (3.7) provides the relations between punching distance (c') and several constituent parameters. Fig. 3.2 shows such an example, i.e. the punching distance (c') normalized by half of fiber length (c) as a function of fiber aspect ratio (c/a). Figure 3.2 implies that the punching along the fiber axis would become more difficult as fiber aspect ratio increases. In this case, the punching is more likely to take place along the direction transverse to the fiber axis, as discussed in Section 3.3. The relaxation by dislocation punching results in lowering the stress field in around a short fiber. Table 3.1 shows the normal stress components (σ_{11} , σ_{22} and σ_{33}) normalized by 2μ where μ is the matrix shear modulus for relaxed (after punching) stage, Fig. 3.3(a) and non-relaxed (before punching) stage, Fig. 3.3(b). The stresses are calculated for several locations: within a fiber (A), just outside the fiber at equator (B) and just outside the fiber-ends (C). Table 3.1 indicates that the magnitude of the stress field in and around a short fiber in the relaxed stage indeed is smaller than that of the non-relaxed stage. The data used to compute the stress field (Table 1) and punching distance (Fig. 3.2) referred to SiC short fiber/Al system and are given elsewhere (Taya and Mori, 1987).

Table 3.1. Stress at points A, B and C (see Fig. 3.3)

$\frac{\sigma_{ij}}{2\mu} \times 10^{-2}$	For relaxed state			For non-relaxed state		
	11	22	33	11	22	33
A	-0.225	-0.225	-0.84	-0.245	-0.245	-1.184
B	-0.225	0.198	0.069	-0.245	0.213	0.119
C	0.0035	0.0035	-0.84	-0.149	-0.149	-0.184

Dunand and Mortenson modified the above model to account for partial relaxation by dislocation punching along the fiber axis. The eigenstrains based on this model are given by eqs. (3.5) and (3.6) where (3,3) element in \underline{e}^{*1} is replaced by $(1-\chi) e_T$ and that in \underline{e}^{*2} by χe_T

$\left(\frac{c}{c'}\right)$, where χ denotes the fraction of the misfit strain to be relaxed by dislocation punching. The modified model of Dunand and Mortenson appears to explain well their experimental results.

3.2 Dislocation Punching From a Spherical Particle

The dislocation punching from a spherical particle was studied both theoretically and experimentally by Taya et al. (1991). It is expected that the direction of dislocation punching from a spherical particle is spherically symmetric. Fig. 3.4(a), (b) and (c) show the CTE mismatch strain adhered to the particle-matrix interface as dislocation loops before punching, after punching, and the rearrangement of the dislocation loops, respectively. The dislocation punching shown by Fig. 3.4(b) should take a form of glide motion as illustrated by Fig. 3.5, i.e. during punching an edge dislocation is degenerated to two partial edge dislocations which move along the glide planes, and after punching, two edge dislocations are formed to one edge dislocation arrayed in a spherically symmetric manner. The eigenstrains representing the case of Fig. 3.4(b) (or Fig. 3.4(c)) are isotropic in a domain of punched spherical region including the particle (Ω_2) and given by

$$\underline{e}^{*2} = \begin{Bmatrix} e_T \left(\frac{c}{c''}\right)^3 & 0 & 0 \\ 0 & e_T \left(\frac{c}{c''}\right)^3 & 0 \\ 0 & 0 & e_T \left(\frac{c}{c''}\right)^3 \end{Bmatrix} \quad (3.9)$$

The criterion for dislocation punching is given by eq. (3.7). c' and c'' are defined by Fig. 3.4(b). The geometry after punching in a spherical particle MMC is shown schematically in Fig. 3.6 where (a) and (b) denote the case of extensive and less extensive punching, respectively. It is noted here that in the case of extensive punching, Fig. 3.6(a), the punched dislocations located at the boundary of Ω_2 are canceled out if they are overlapped with adjacent dislocations, resulting in no contribution of *geometrically necessary dislocations* to increase in the matrix flow stress. However, as the *geometrically necessary dislocations* are punched, *statistically stored dislocations* are left out in the wake region ($\Omega_2 - \Omega_1$) since the actual mode of the dislocation punching is not spontaneous, but successive punching of

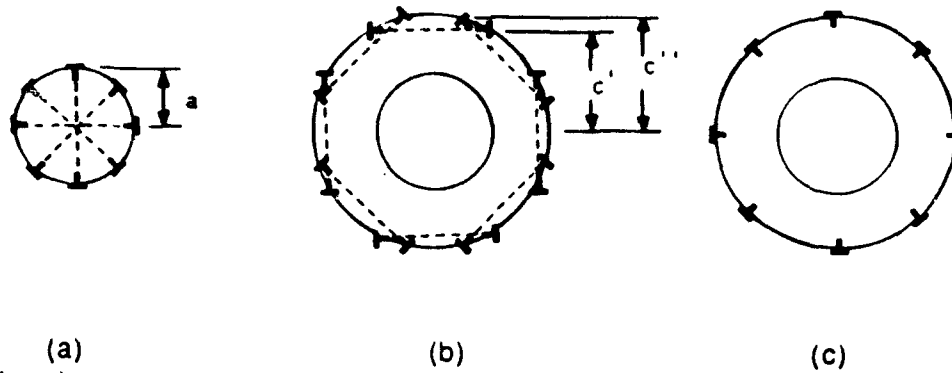


Fig. 3.4 Dislocation punching model used by Taya et al. (1991): (a) CTE mismatch strain ϵ_T adhered to the particle/matrix surface as prismatic dislocation loops, (b) after punching to c' , (c) rearrangement of loops for spherical symmetry.

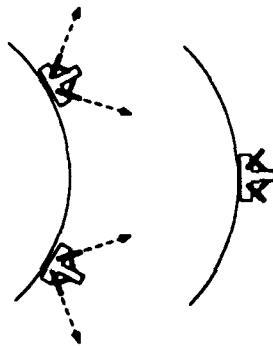


Fig. 3.5 Dissociated dislocations make glide motion and are combined to form a new dislocation.

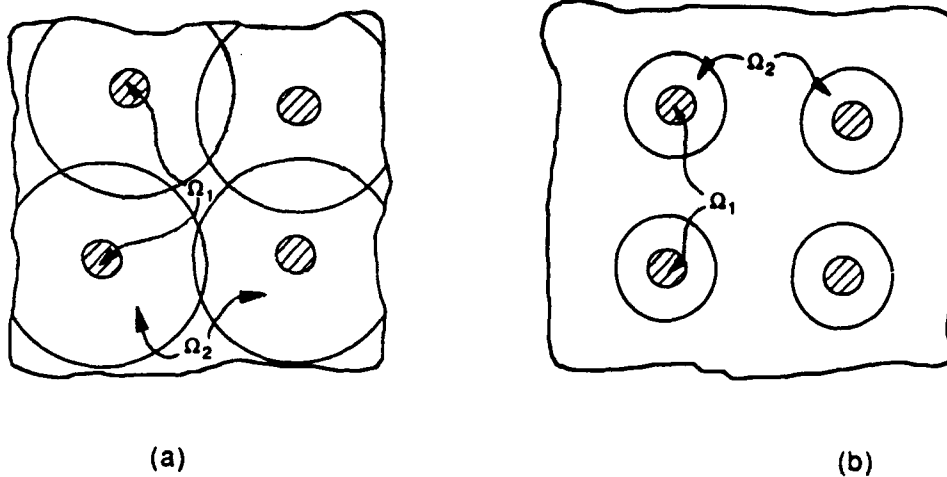


Fig. 3.6 Punched regions in a particle MMC:
(a) for extensive punching resulting in overlapping of the frontal boundaries.
(b) for less extensive punching.

dislocation loops. Thus, for extensive punching, one can expect an increase in matrix flow stress due to the *statistically stored dislocations*.

The formulations of the stress and strain field, and also the strain energy of a composite, are again based on the Eshelby's method and its details are given elsewhere (Taya et al., 1991; Shibata et al., 1992). The average dislocation density for less extensive punching mode, Fib. 3.6(b) is given by

$$\bar{\rho} = \frac{6\epsilon_T f}{ab(1-f)} \quad (3.10)$$

where f is the volume fraction of particles, ϵ_T is CTE mismatch strain, a is the radius of a spherical particle and b is Burgers' vector. A comparison between eqs. (3.3) and (3.10) reveals that the averaged dislocation density in the matrix predicted by the Arseault and Shi model is twice as much as that by the Taya et al. model, if t is set equal to a . In the case of extensive punching, Fig. 3.6(a), the average dislocation density is computed by Shibata et al. (1992) and given by

$$\bar{\rho} = \frac{6fke_T}{\mu b} \ln(f^{-1/3}) \quad (3.11)$$

It is noted that eq. (3.11) was derived by accounting for only *statically stored dislocations*.

In order to predict the yield stress of a particle MMC, one should consider another strengthening mechanism, i.e. back stress strengthening which is to account for resistance of elastic particles against plastically deforming matrix metal. Hence the increase in the composite yield stress over the unreinforced metal is due to two mechanisms: dislocation punching as a result of relaxation of CTE mismatch strain at the interface ($\Delta\sigma_{CTE}$) and back stress ($\Delta\sigma_b$). In order to test the validity of the above strengthening mechanisms, Taya et al. (1991) conducted experiment on SiC particle/6061 Al composite-T4 (SiCp/Al). The mechanical properties of SiCp/Al composite are given in Table 3.2.

Table 3.2. Material Properties

Parameter	Unit	Al Matrix	SiC Particle
Young's modulus	GPa	68.3	427
Yield strength	MPa	97.0	—
Poisson's ratio	1	0.33	0.17
CTE	$\times 10^{-6}$ C	23.6	4.3
Burgers' vector	nm	0.283	—
Average particle radius	μ m	—	5.0

SiCp/Al specimens were solution-treated at 530°C, thus eliminating much of the dislocations induced by processing, then quenched to several different temperatures (T_q): room temperature, 0, -64, and -196°C, followed by tensile testing at these temperatures to measure the yield stresses. The purpose of quenching is to generate given CTE mismatch strain at the interface. Figure 3.7(a) shows the composite yield stresses experimentally obtained (open circle) and predicted by the dislocation punching and backstress strengthening models (filled circle) as a function of temperature change by quenching, $\Delta T = T_q - 530$. In

order to examine as to which strengthening mechanism is dominant, $\Delta\sigma_b$ and $\Delta\sigma_{CTE}$ are plotted in Fig. 3.7(b), indicating that $\Delta\sigma_{CTE}$ is larger than $\Delta\sigma_b$. Namely strengthening due to dislocation punching is dominant.

3.3 Dislocation Punching From a Continuous Fiber.

As the results of Fig. 3.2 suggest, the dislocation punching from a continuous fiber in a continuous fiber MMC is more likely to take place along the transverse direction (transverse to the fiber axis). This was studied analytically by Shibata et al. (1992). The eigenstrains after punching are given by

$$\underline{e}^{*1} = \left\{ \begin{array}{ccc} 0 & 0 & 0 \\ 0 & 0 & 0 \\ 0 & 0 & e_T \end{array} \right\} \text{ in } \Omega_1 \quad (3.12)$$

$$\underline{e}^{*2} = \left\{ \begin{array}{ccc} e_T \left(\frac{a}{R} \right)^2 & 0 & 0 \\ 0 & e_T \left(\frac{a}{R} \right)^2 & 0 \\ 0 & 0 & 0 \end{array} \right\} \text{ in } \Omega_2 \quad (3.13)$$

where Ω_1 and Ω_2 denote the domains of the fiber and the punched region encompassing the fiber, respectively; a and R are the radii of the fiber and the punched region, respectively. By using the Eshelby's model to compute the total elastic energy of the composite and the criterion for punching, eq. (3.7), and the dissipation energy for punching, one can obtain the punching distance (radius of the punched region) \bar{R} as

$$\bar{R} = a \left\{ \frac{(1 + 2\nu) \mu e_T}{2(1 - \nu) k} \right\}^{1/2} \quad (3.14)$$

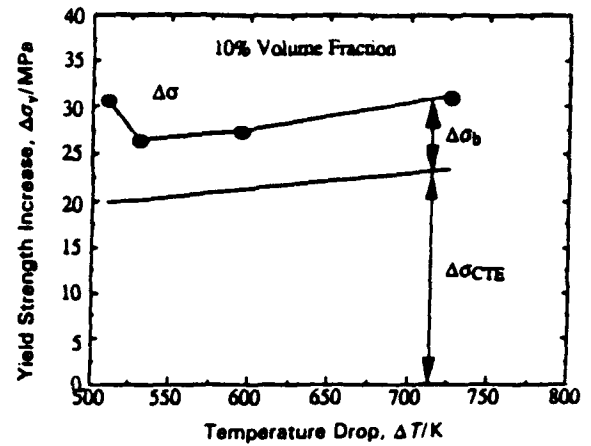
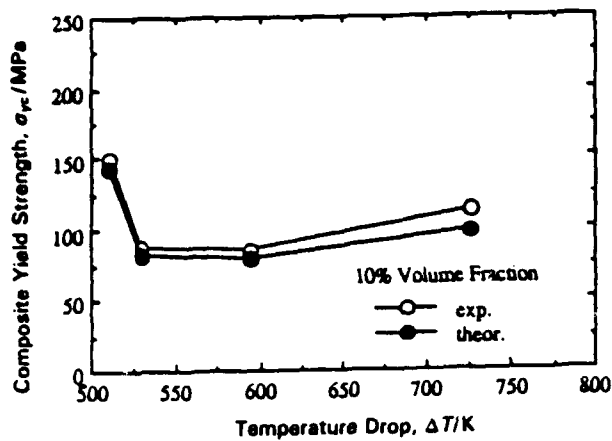
where μ and k are the shear modulus and friction stress of the matrix metal, respectively. Equation (3.14) was obtained for a single continuous fiber embedded in an infinite matrix. The result of the punching distance \bar{R} for a continuous fiber MMC with finite volume fractions of fiber can be obtained similarly (Shibata et al. 1992). It is noted here that the yield criterion based on Hill's model

$$|\sigma_r - \sigma_\theta| = 2k \quad (3.15)$$

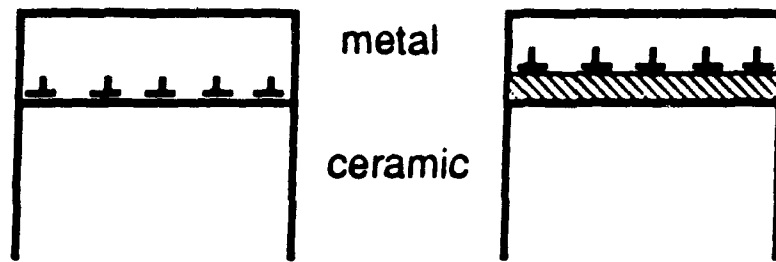
is not satisfied within the plastic domain ($\Omega_2 - \Omega_1$) where σ_r and σ_θ are radial and circumferential stress components. However, the average stress across the boundary of Ω_2 is defined by

$$\bar{\sigma}_{ij} = \lim_{\epsilon \rightarrow 0} \{ \sigma_{ij}(R - \epsilon) + \sigma_{ij}(R + \epsilon) \} / 2 \quad (3.16)$$

satisfy the yield condition, eq. (3.15) which gives rise to eq. (3.14).



(a) (b)
 Fig. 3.7 Composite yield stress vs. temperature change by quenching: (a) a comparison between the experiment and the prediction based on the dislocation punching model, (b) breakdown of the increase in the composite yield stress indicating strengthening due to dislocation punching ($\Delta\sigma_{CTE}$) dominant over that due to back stress ($\Delta\sigma_b$).



(a) (b)
 Fig. 3.8 Dislocation punching model for a thin metal coating/ceramic substrate system: (a) before punching, (b) after punching to distance z .

3.4 Dislocation Punching From a Planar Interface

The generation of dislocations at the interface of a thin coating/substrate system has been studied in terms of critical thickness of the coating-misfit strain relation (Matthews and Blakesee, 1974; Freund, 1987). These studies are aimed at epitaxial layers and the order of the critical thickness is normally much smaller, 10 ~ 100 nm. For a coated substrate system with non-epitaxial interface and intermediate coating thickness, the results of the above studies are not applicable.

Here we consider a metal thin coating/ceramic substrate with CTE driven misfit strain at the interface. The CTE misfit strain is defined by

$$\begin{aligned} e_{ij}^* &= e^* \delta_{ij} \\ e^* &= (\alpha_c - \alpha_s) \Delta T \end{aligned} \quad (3.17)$$

where α_c and α_s are CTE of the coating and substrate, respectively, δ_{ij} is knocker's delta and ΔT is temperature change. First we examine the stress field before punching Fig. 3.8(a) and then the case of punching to some distance, Fig. 3.8(b).

It is assumed in this model that the thickness of coating is reasonably thin, so that out-of-plane stress component in the coating (σ_{33}) can be ignored, and also that the plane strain condition be held for in-plane directions, x_1 - and x_2 -axes within the coating.

Before Punching

By the assumption of plane strain along the x_1 - and x_2 -axes,

$$e_{11} = e_{22} = -e^* \quad (3.18)$$

where e_{ij} is elastic strain component. Hooke's law with $\sigma_{33} = 0$ gives rise to

$$\begin{aligned} e_{11} &= \frac{\sigma_{11}}{E} - \frac{\nu}{E} \sigma_{22} \\ e_{22} &= \frac{\sigma_{22}}{E} - \frac{\nu}{E} \sigma_{11} \\ e_{33} &= -\frac{\nu}{E} (\sigma_{11} + \sigma_{22}) \end{aligned} \quad (3.19)$$

where ν is the Poisson's ration of the coating.

From eqs. (3.18) and (3.19) we obtain the in-plane stresses and out-of-plane strain as

$$\begin{aligned} \sigma_{11} = \sigma_{22} &= -\frac{E e^*}{(1 - \nu)} \\ e_{33} &= \frac{\nu}{1 - \nu} e^* \end{aligned} \quad (3.20)$$

Punching to Distance z

Assuming that the dislocation punching took place with its frontal boundary located Z from the interface, Fig. 3.8(b), we shall calculate the stress and strain field within the punched region (Ω_1) and elastic region (Ω_0) and also the condition for punching.

in Elastic Region (Ω_0):

Stress σ_{ij} and strain e_{ij} are the same as those in the coating before punching, i.e. given by eq. (3.20).

in Plastic Region (Ω_1):

Denoting plastic strain in the punched region by e_{ij}^P and using the plane strain condition in the $x_1 - x_2$ plane and incompressibility of plastic strain, one arrives at

$$\begin{aligned} e_{11}^P &= e_{22}^P = -e_T \\ e_{33}^P &= 2e_T \end{aligned} \quad (3.21)$$

and

$$\sigma_{ij} = 0 \quad (3.22)$$

It is noted that stresses in Ω_1 are all zero due to complete relaxation.

Computation of Elastic Energy U and Plastic Work W

The elastic energy per unit width along the x_2 -axis is given by

$$U = \frac{1}{2} \sigma_{ij} e_{ij} (\ell - z) \quad (3.23)$$

A substitution of eqs. (3.18) and (3.20) into (3.23) yields

$$U = \frac{E e_T^2 (\ell - z)}{(1 - \nu)} \quad (3.24)$$

The plastic work per unit width, W is given by

$$W = \sigma_{ij} e_{ij}^P z \quad (3.25)$$

by using eq. (3.21) and $\sigma_{11} = \sigma_{22} = \sigma_y$ (yield stress), W is reduced to

$$W = 4k e_T z$$

where $\sigma_y = 2k$ was used and k is yield stress in shear. The punching criterion is given by

$$-\frac{\partial U}{\partial Z} \geq \frac{\partial W}{\partial Z} \quad (3.26)$$

where the left term represents the driving force for punching while the right is the retarding force against punching.

By substituting eqs. (3.24) and (3.25) into (3.26) we obtain the condition for punching

$$e_T \geq \frac{4k(1-\nu)}{E} \quad (3.27)$$

Inequality (3.27) can be derived by invoking the yield criterion across the frontal boundary of the punched region, i.e. the interface between Ω_0 and Ω_1 , Fig. 3.8(b). The average stresses across the boundary are calculated by using eqs. (3.16), (3.20) and (3.22).

$$\bar{\sigma}_{11} = \bar{\sigma}_{22} = -\frac{E e_T}{2(1-\nu)} \quad (3.28)$$

which is substituted into Hill's yield criterion

$$\left| \bar{\sigma}_{33} - \bar{\sigma}_{11} \right| \geq 2k \quad (3.29)$$

A substitution of eq. (3.28) and $\sigma_{33} = 0$ into (3.29) leads to (3.27).

4. Analytical Study II: Creep and Thermal Cycling Creep of Metal Matrix Composites

4.1 Background

Dimensional stability in high temperature use environments is crucial for many metal matrix composite (MMC) applications. While MMCs reinforced by ceramic fibers offer creep resistance superior to the unreinforced metal, it is well known that the combination of relatively small applied stresses and cyclic thermal loading can result in creep rates far in excess of those observed during isothermal high temperature creep. Even in the absence of an applied stress, a detrimental dimensional change has been observed in a number of thermal cycled metal matrix composite systems. These effects are attributed to internal stresses that are developed during thermal cycling due to the coefficient of thermal expansion mismatch between the matrix and fibers. Creep and thermal cycling creep are among the least understood aspects of the deformation of MMCs, but are of utmost importance for the development of MMCs for high temperature structural applications.

Creep in short fiber metal matrix composites has been studied both experimentally and theoretically by numerous researchers. A comprehensive review is not attempted here, but the reader is referred to recent reviews by Taya (1991) and Taya et al. (1991). Recent works regarding modeling of creep of short fiber composites include Zhu and Weng (1989, 1990a, 1990b), Wang and Weng (1992), and Pan and Weng (1992). In these works, Eshelby's (1957) equivalent inclusion method was combined with the Mori-Tanaka (1973) mean field approach to estimate the stress redistribution due to an incremental creep of the metal matrix and the subsequent creep deformation of the composite. A similar approach was used by Taya and Mori (1987) to model creep of a short fiber MMC during the high temperature hold stage of a cyclic thermal loading. With regards to thermal cycling and thermal cycling creep of short fiber MMCs, Derby (1991) and Taya et al. (1993) have recently provided a comprehensive review of the literature and a list of references with regards to both experimental and theoretical aspects can be found therein. Other recent contributions have been directed at understanding the effects of reinforcement geometry on the thermal cycling creep of short fiber MMCs through the development of idealized models and the application of finite element methods (Zhang et al., 1991; Chen and Daehn, 1991; Povirk et al., 1992).

During isothermal creep of a MMC, degradation of the fiber matrix interface, often in the forms of void nucleation and growth followed by debonding, has been observed to lead to tertiary creep and creep fracture (Nieh, 1982; Morimoto et al., 1988; Dragone et al., 1991; Pandey et al., 1993). The accumulation of inelastic strain during thermal cycling has also been observed to be accompanied by the development of interfacial damage in the forms of porosity, debonding, and an attached reaction zone containing radial cracks (Echigoya et al., 1990). These damage processes, in both isothermal and thermal cycling creep further accelerate the inelastic strain accumulation and thus it is important to understand the evolution of damage and its effect on the overall response of the MMC.

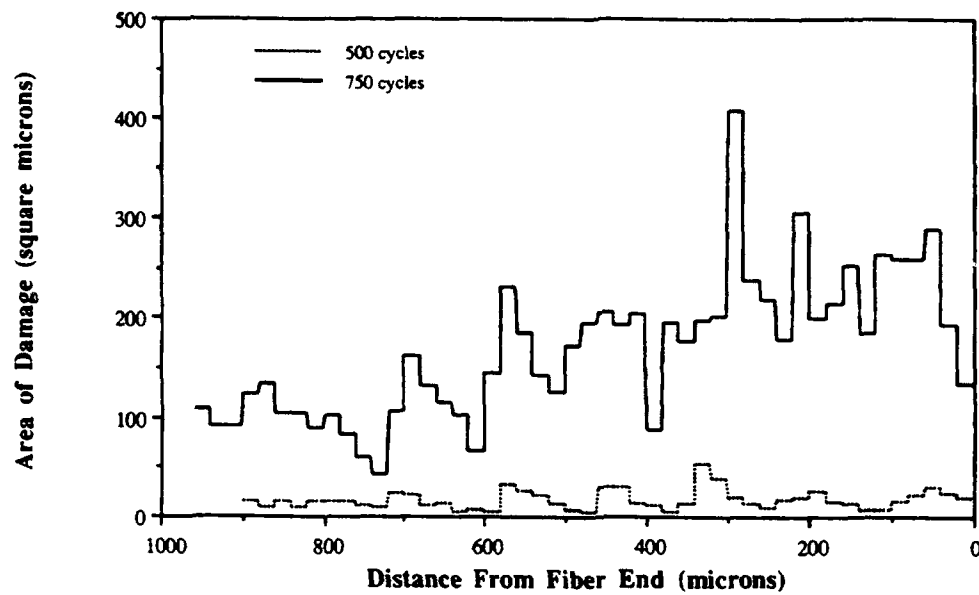
This work is a continuation of the authors' study of creep, thermal cycling, and creep thermal cycling (thermal cycling with an applied stress) of metal matrix composites. In particular, a micromechanics-based analytical approach is proposed to model creep and thermal cycling creep of short fiber MMCs with interfacial damage. The approach is an extension of the analyses of Taya et al. (1991) for creep, Taya and Mori (1987) for thermal cycling, and Dunn and Taya (1992) for creep thermal cycling of MMCs and is based on the combination of Eshelby's (1957) equivalent inclusion method and the Mori-Tanaka (1973)

mean field approach (see for example Mura, 1987). Interfacial damage is modeled through a hybrid approach where the composite is assumed to contain both perfectly bonded fibers and fibers with damaged interfaces. The evolution of damage is described by an arbitrary statistical distribution. Efforts to correlate the statistical distribution of interfacial damage with experiment are currently underway and the results will be subsequently reported.

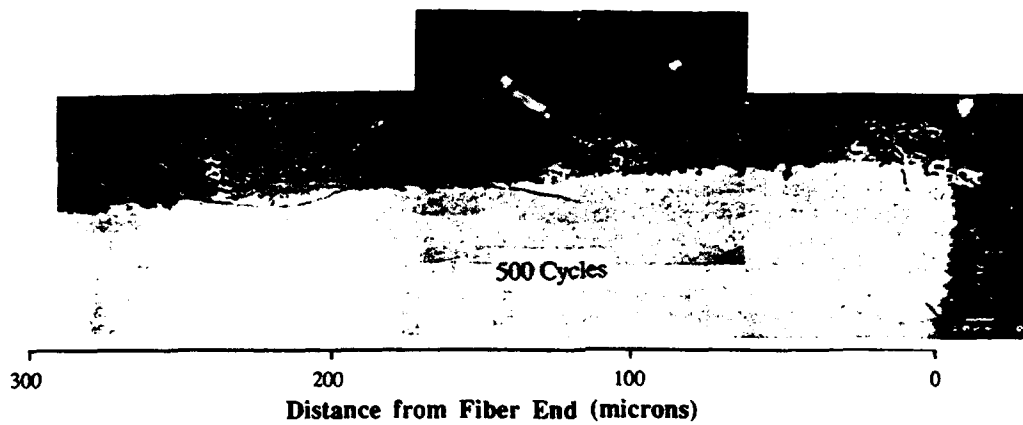
4.2 Analytical Model

It is assumed that initially all fibers are perfectly bonded to the matrix. At some point during the creep or thermal cycling creep loading, though, interfacial damage begins to occur. The effect of the damage is a loss in the ability to effectively transfer load from the matrix to the fibers. When damage has occurred, it is assumed that the aligned short fiber and matrix are still in mechanical contact except at and near the poles of the fibers. This characterization is based on numerous reports from the literature regarding debonding during creep and a microscopy study of thermal cycled W/FeCrAlY short fiber composites of which a typical micrograph is shown in Fig. 4.1 (Armstrong et al., 1991). The fiber-matrix interface is assumed to be stress free in the x_3 direction but not in the x_1 and x_2 direction except in the vicinity of the fiber ends. This assumption seems reasonable when the interface between the short fiber is in tension, but may not be as valid when the stress field at the interface is compressive. These implications will be further discussed in the following section. The stress field in the debonded fibers is analyzed by following the approach proposed by Tanaka et. al. (1970) to model the stress distribution in a spherical particle after cavitation. The stress field in the debonded fibers is simulated by that of a fictitious fiber with anisotropic moduli of $C_{ijkl}^d = 0$ with the exception of $C_{1111}^d = C_{2222}^d$ and $C_{1122}^d = C_{2211}^d$. It is noted that this reduction in moduli is only valid for the case considered here, aligned short fibers subjected to uniaxial mechanical loading along the axis of the fiber.

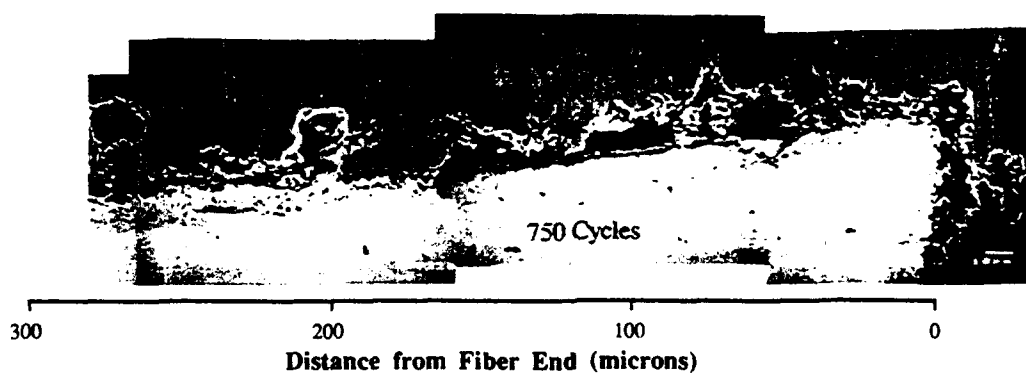
In this section, the response of a composite containing two types of short fibers (perfectly bonded and debonded) will be obtained. The debonded fibers are assumed to be described as discussed in the previous section and the criterion for progressive debonding will then be discussed in the following section. The domain of the analytical model, shown in Fig. 4.2, consists of an infinite metal matrix containing a random distribution of both perfectly bonded and debonded aligned short fibers. The domains of the entire composite and of the bonded and debonded fibers are denoted by D , Ω_b , and Ω_d respectively, and that of the matrix is thus denoted by $D - \Omega_b - \Omega_d$. The elastic moduli of the matrix and two types of fibers are C_m , C_b , and C_d , respectively. It is noted that C_m and C_b are defined in the standard manner while C_d has been defined in Section 2. In this work, bold and underscored symbols represent tensorial quantities. Both types of fibers are modeled as ellipsoidal inhomogeneities (prolate spheroids) and for simplicity both the matrix and fibers are assumed to be initially isotropic in stiffness and thermal expansion. To model the creep response of the composite, a constant applied stress, $\underline{\sigma}_0$, is assumed and in addition the idealized time-temperature thermal cycle shown in Fig. 4.3 is assumed during thermal cycling creep. It is assumed that the fibers deform elastically and the matrix is capable of elastic/plastic/creep deformations. The material properties, with the exception of the yield stress and creep properties of the matrix, are assumed independent of temperature. This assumption can be relaxed, however, and the analysis can be easily implemented in an incremental manner.



(a)



(b)



(c)

Fig. 4.1 Debonding of the interface in a short W fiber/FeCrAlY matrix composite subjected to thermal cycling : (a) area of interfacial damage, (b) SEM photomicrograph at N = 500 and (c) N = 750.

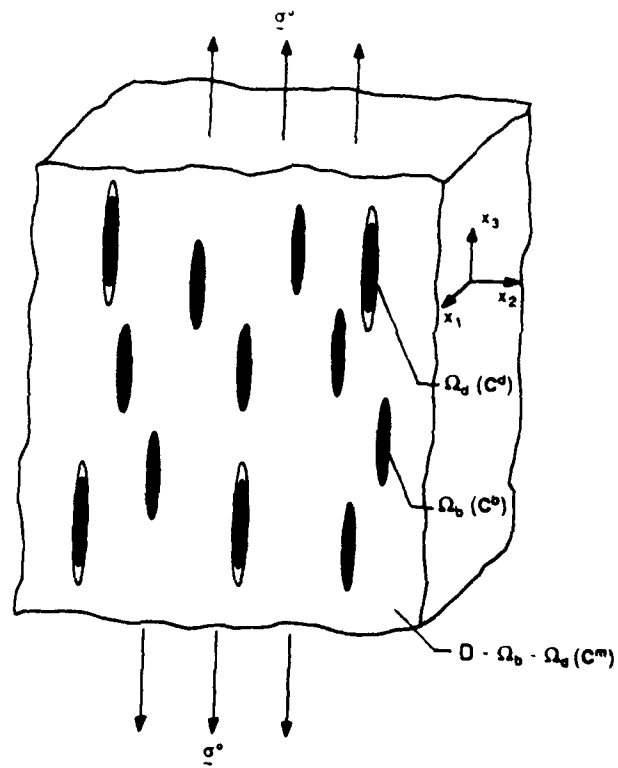


Fig. 4.2 Analytical model.

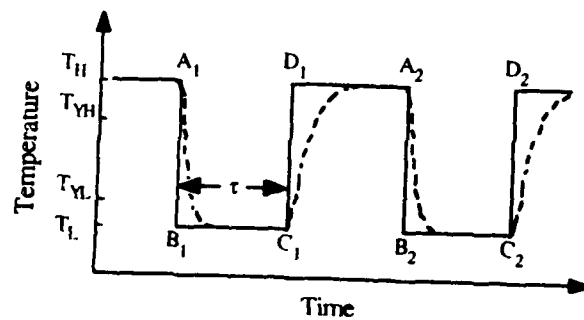


Fig. 4.3 Idealized temperature-time relation.

4.2.1 Creep of Short Fiber Metal Matrix Composites

Response to the Applied Stress

The overall response of the composite to the uniform applied stress, σ^o , (with corresponding strain e^o) can be estimated by the use of Eshelby's (1957) equivalent inclusion method coupled with the Mori-Tanaka (1973) mean field approach as applied to a three-phase composite (Taya and Chou, 1981). Through the equivalent inclusion method, the stress in a single representative perfectly bonded fiber is given by:

$$\sigma^o + \sigma^b = C_b \cdot [e^o + \bar{e} + e^b] = C_m \cdot [e^o + \bar{e} + e^b - e^{*ob}] \quad (4.1)$$

That in a single representative debonded fiber is given by:

$$\sigma^o + \sigma^d = C_d \cdot [e^o + \bar{e} + e^d] = C_m \cdot [e^o + \bar{e} + e^d - e^{*od}] \quad (4.2)$$

where \bar{e} is the volume averaged disturbance strain in the matrix and e^i and e^{*oi} are the disturbance strain and fictitious eigenstrain in the i th domain ($i=b,d$) required for the simulation of the inhomogeneities by the equivalent inclusion, respectively. These can be expressed as:

$$\langle \sigma \rangle_m = C_m \cdot \bar{e} \quad (4.3)$$

$$e^i = S \cdot e^{*oi} \quad (4.4)$$

where S is Eshelby's (1957) tensor and $\langle \sigma \rangle_m$ is the volume average of the disturbance stress (due to both Ω_b and Ω_d) in the matrix. Eshelby's tensor is a function only of the shape of the inhomogeneity and the elastic moduli (Poisson's ratio for isotropic materials) of the matrix and thus is the same for both the bonded and debonded fibers. It is not difficult to show that the volume average of σ^i over the entire composite vanishes which results in:

$$\bar{e} = (S - I) \cdot [f_b e^{*ob} + f_d e^{*od}] \quad (4.5)$$

where f is the volume fraction of fibers. After some manipulation, eqs. (4.1) - (4.5) yield $\langle \sigma \rangle_m$ which can be used to obtain the average stresses and strains in each phase and in the composite. Of particular interest are the average stress in the *matrix*, $\langle \sigma \rangle_m^{\sigma^o}$, and the average strain of the *composite*, $\langle e \rangle_c^{\sigma^o}$, which can be expressed as:

$$\langle \sigma \rangle_m^{\sigma^o} = R(C_m, C_b, C_d, S, f_b, f_d) \cdot \sigma^o \quad (4.6)$$

$$\langle e \rangle_c^{\sigma^o} = H(C_m, C_b, C_d, S, f_b, f_d) \cdot \sigma^o \quad (4.7)$$

Response to an Incremental Creep

An incremental creep of the matrix, de^C , results in a redistribution of stress from the creeping matrix to the elastic fibers, but as noted by Weng (1987), is itself a stress-free process. Thus, Eshelby's equivalent inclusion method can be used to estimate the stress redistribution due to an incremental creep:

$$d\sigma^b = C_b \cdot [d\bar{\epsilon} + de^b + de^C] = C_m \cdot [d\bar{\epsilon} + de^b - de^C b] \quad (4.8)$$

$$d\sigma^d = C_d \cdot [d\bar{\epsilon} + de^d + de^C] = C_m \cdot [d\bar{\epsilon} + de^d - de^C d] \quad (4.9)$$

de^C and de^{C^i} are the incremental creep of the matrix and the corresponding incremental eigenstrain and all other stress and strain increments are analogous to their previous definitions in eqs.(4.1) and (4.2). By a development similar to that used to obtain eqs. (4.6) and (4.7), the average stress increment in the matrix and strain increment of the composite due to an incremental creep of the matrix, de^C , can then be expressed as:

$$\langle d\sigma \rangle_m^{e^C} = U(C_m, C_b, C_d, S, f_b, f_d) \cdot de^C \quad (4.10)$$

$$\langle de \rangle_c^{e^C} = V(C_m, C_b, C_d, S, f_b, f_d) \cdot de^C \quad (4.11)$$

where due to the assumption of incompressibility and symmetry of deformation, de^C is given by $de^C = [-d\epsilon^C/2, -d\epsilon^C/2, d\epsilon^C, 0, 0, 0]^T$.

For simplicity, the creep rate of the matrix is assumed to be described by the Mises J_2 creep flow rule Odqvist (1974):

$$\dot{\epsilon}_{ij}^C = k J_2^m < \sigma_{ij}^i >_m \quad \text{or} \quad \dot{\epsilon}^C = \pm A | \sigma_m |^n \quad (4.12)$$

where $d\epsilon^C = \dot{\epsilon}^C dt$. In eq. (4.12), J_2 , $< \sigma_{ij}^i >_m$, and σ_m are the second invariant, deviatoric components, and the flow stress of the average stress in the matrix and are all computed in the standard manner and as usual the (+) or (-) sign corresponds to the sign of the flow stress. The second of eqs. (4.12) results when axisymmetric deformation is present as will be assumed here. During creep of the matrix, the average stress in the matrix can be determined by integration of eq. (4.12) with the initial condition of eq. (4.6). From the average stress in the matrix, the flow stress is determined as a function of ϵ^C , which in turn is a function of time. The flow stress can then be substituted into the power law of eq. (4.12) to yield a first order nonlinear ordinary differential equation in ϵ^C of the form:

$$\dot{\epsilon}^C = A [(a \sigma^o + b \epsilon^C)]^n \quad (4.13)$$

For the applied uniaxial stress along the fiber (x_3) axis, the solution to the ODE of eq. (4.13) is:

$$\epsilon^C(t) = \frac{1}{C} \left\{ (a \sigma^o)^{(1-n)} + (1-n) Abt \right\}^{1/(1-n)} - \frac{a}{b} \sigma^o \quad (4.14)$$

where a and b are functions of C_m , C_b , C_d , S , f_b , and f_d . It is noted that n is assumed to be independent of stress. This assumption can easily be relaxed to include the functional dependence of n on stress, however the resulting differential equation must then be integrated numerically. Finally, the creep strain of the composite is related to that of the matrix, $\epsilon^C(t)$, through eq. (4.11).

Progressive Debonding

The model developed thus far is valid for an arbitrary combination of short fibers with bonded and damaged interfaces. The goal of this approach is to predict the progression of damage and its subsequent effect on the behavior of the composite. In other words, it is desired to understand how f_d , which is initially zero, evolves with the accumulation of inelastic strain. Here an attempt is made to relate f_d to the strength of the fiber-matrix interface through a statistical distribution function, the form of which will be obtained from careful experiment. Here it is assumed that the evolution of f_d can be described by the use of a three-parameter Weibull distribution as:

$$f_d = F(\sigma_{ib}) f_{tot} \quad (4.15)$$

where f_{tot} is the total volume fraction of fibers, i.e., $f_{tot} = f_b + f_d$ and $F(\sigma_{ib})$ is the cumulative density function:

$$F(\epsilon_{tot}) = 1 - \exp \left[- \left(\frac{\sigma - \sigma_{ib}}{\theta - \sigma_{ib}} \right)^b \right] \sigma \geq \sigma_{ib} \quad (4.16)$$

where b , σ_{ib} , and θ are the shape parameter, guaranteed value of σ (the stress σ_{33} at the interface), and the scale parameter respectively. Thus, f_d is a function of σ_{33} which is in turn a function of time as σ_{33} increases as stress is redistributed from the creeping matrix to the elastic fibers. Equation (4.13) is still valid, but now it must be integrated numerically as a and b are now functions of time. Although a Weibull distribution is used here, it is emphasized that the proposed model is easily able to handle an arbitrary statistical distribution.

4.2.2 Thermal Cycling Creep of Short Fiber Metal Matrix Composites

In this section the development of an approach to model thermal cycling creep of short fiber metal matrix composites is outlined. The model extends that of Dunn and Taya (1992) for thermal cycling creep of undamaged short fiber composites to model the effects and progression of interfacial damage in the same manner as was done with regards to isothermal creep in the previous section. Thus, only a brief outline of the approach will be given and the reader is referred to Dunn and Taya (1992) for additional details.

The composite subjected to thermal cycling creep is assumed to be subjected a constant applied stress and then the idealized thermal cycle shown in Fig. 4.3. The initial response to the applied stress at A_1 of Fig. 4.3 is identical to that described in Section 4.2.1. During cooling (A_1 to B_1), the composite is subjected to the uniform temperature drop $\Delta T = T_L - T_H$ which induces a non-uniform thermal stress field in the composite due to the mismatch in coefficients of thermal expansion (CTEs) between the matrix and fibers. By use of the

equivalent inclusion method, the inhomogeneities with thermal strain $e^{\Delta T}$ can be simulated by equivalent inclusions with fictitious eigenstrains $e^{*\Delta T}$ to yield:

$$\sigma^b = C_b \cdot [\bar{\epsilon} + e^b - e^{\Delta T}] = C_m \cdot [\bar{\epsilon} + e^b - e^{*\Delta T} b] \quad (4.17)$$

$$\sigma^d = C_d \cdot [\bar{\epsilon} + e^d - e^{\Delta T}] = C_m \cdot [\bar{\epsilon} + e^d - e^{*\Delta T} d] \quad (4.18)$$

where $e^{\Delta T} = (\alpha_b - \alpha_m) \Delta T$ is a result of the mismatch between the CTEs of the matrix, α_m , and the bonded and debonded fibers, $\alpha_b = \alpha_d$.

In a manner similar to that used to obtain eqs. (4.6) and (4.7), the average thermoelastic stress, $\langle \sigma \rangle_m^{\Delta T}$, and strain, $\langle e \rangle_c^{\Delta T}$, due to $e^{\Delta T}$ can be obtained as:

$$\langle \sigma \rangle_m^{\Delta T} = P(C_m, C_b, C_d, S, f_b, f_d, \alpha_b, \alpha_m) \Delta T \quad (4.19)$$

$$\langle e \rangle_c^{\Delta T} = Q(C_m, C_b, C_d, S, f_b, f_d, \alpha_b, \alpha_m) \Delta T \quad (4.20)$$

It is assumed that the temperature drop from T_H to T_L is sufficient to initiate uniform yielding of the matrix metal. The critical temperature change at which yielding of the matrix begins, $\Delta T_{cr}^L = T_H - T_{YL}$, can be found by subjecting the average thermoelastic stress in the matrix to the yield criterion:

$$3/2 \langle \sigma' \rangle_m \cdot \langle \sigma' \rangle_m = \sigma_{YL}^2 \quad (4.21)$$

where $\langle \sigma' \rangle_m$ is the deviatoric portion of the thermoelastic stress and σ_{YL} is the yield stress of the matrix at T_L . When the applied stress is uniaxial along the x_3 -axis, the critical temperature change required for yielding of the metal matrix can then be expressed as:

$$\Delta T_{cr} = \frac{\sigma_{YL} - (R_{33} - R_{31}) \sigma^o}{P_3 - P_1} \quad (4.22)$$

The temperature drop from T_{YL} to T_L will then result in plastic deformation of the matrix.

To compute the plastic deformation, it is assumed that the temperature drop from T_{YL} to T_L induces a uniform plastic strain, e^{PL} , in the matrix and that the matrix is a non-hardening material. The assumption of a uniform plastic strain in the matrix neglects the effects of microyielding that is known to occur near the fiber-matrix interface upon relatively low temperature changes. It is the average stress field in the matrix, however, that is believed to influence the *macroscopic* deformation of the composite and this is the basis for the proposed approach. The uniform plastic strain, e^{PL} , is assumed to satisfy the incompressibility requirement $e_{ii}^{PL} = 0$ and as a result of symmetry (of both loading and microstructure) can be expressed as $e^{PL} = \epsilon^{PL} [-1/2, -1/2, 1, 0, 0, 0]^T = \epsilon^{PL} K$. The stress field due to e^{PL} can be computed by use of Eshelby's equivalent inclusion method where $e^{\Delta T}$ and $e^{*\Delta T}$ in eqs. (4.17) and (4.18) are replaced by $-e^{PL}$ and e^{*PL} respectively. The plastic strain, e^{PL} , can be determined by applying the yield criterion to the unknown *total* stress existing at T_L .

(B₁). With the plastic strain, ϵ^{PL} , known, the average stress in the matrix and strain of the composite at B₁ can be expressed as:

$$\langle \sigma \rangle_m^{B_1} = \langle \sigma \rangle_m^{\sigma^0} + \langle \sigma \rangle_m^{\Delta T} + \langle \sigma \rangle_m^{\epsilon^{PL}} = R \cdot \sigma^0 + P \cdot \Delta T + U \cdot \epsilon^{PL} \quad (4.23)$$

$$\langle \epsilon \rangle_c^{B_1} = \langle \epsilon \rangle_m^{\sigma^0} + \langle \epsilon \rangle_m^{\Delta T} + \langle \epsilon \rangle_m^{\epsilon^{PL}} = H \cdot \sigma^0 + Q \cdot \Delta T + V \cdot \epsilon^{PL} \quad (4.24)$$

where U and V are defined by eqs. (4.10) and (4.11). During the low temperature plateau, B₁ → C₁, no further deformations are assumed to occur and thus eqs. (4.8) and (4.9) describe the state of the composite at C₁.

The thermoelastic stress developed during the heating process, C₁ → D₁, is equal in magnitude but of opposite sign to that generated upon cooling. Reverse yielding, resulting in plastic strains ϵ^{PH} , may or may not occur depending on the values of σ_{YH} , the yield stress at T_H (σ_{YH}), and ΔT . The state of the composite at D₁ can be determined in the same manner as that upon cooling to yield:

$$\langle \sigma \rangle_m^{D_1} = R \cdot \sigma^0 + U \cdot [\epsilon^{PL} + \epsilon^{PH}] \quad (4.25)$$

$$\langle \epsilon \rangle_c^{D_1} = H \cdot \sigma^0 + V \cdot [\epsilon^{PL} + \epsilon^{PH}] \quad (4.26)$$

During the high temperature plateau, D₁ → A₂, it is assumed that the flow stress existing at T_H (D₁) is further relaxed by bulk creep of the matrix. For simplicity, it is assumed that the creep properties of the composite matrix are the same as those of the unreinforced matrix alloy. Eshelby's equivalent inclusion method can be used to estimate the stress redistribution due to an incremental creep in the same manner as described in Section 4.2.1. Again the creep rate of the matrix is assumed to be described by eq. (4.12) which is integrated in the same manner outlined in Section 4.2.1 but now with the initial conditions of eq. (4.26) to provide the creep strain at the end of the high temperature plateau ($t = \tau$). Once $\epsilon^C(\tau)$ is obtained the overall state of the composite is:

$$\langle \sigma \rangle_m^{A_2} = R \cdot \sigma^0 + U \cdot [\epsilon^{PL} + \epsilon^{PH} + \epsilon^C(\tau)] \quad (4.27)$$

$$\langle \epsilon \rangle_c^{A_2} = H \cdot \sigma^0 + V \cdot [\epsilon^{PL} + \epsilon^{PH} + \epsilon^C(\tau)] \quad (4.28)$$

The stress-strain-time histories during the second and subsequent thermal cycles are computed in the same manner as that of the first thermal cycle except for the provision of a possible non-zero residual stress at A₂ which is easily accommodated. It turns out that the flow stress at the end of each subsequent thermal cycle is then the same as that at the end of the first.

Finally, a statistical distribution can be implemented to describe the progression of damage in a manner similar to that in Section 4.2.1. For the calculations presented in the following section, a three-parameter Weibull distribution is again used where here the cumulative density function is assumed to be a function of the accumulated inelastic strain.

It is reiterated that the form of the statistical distribution has only been assumed and its precise form will be determined from careful experimental efforts which are presently underway. It is noted that the fiber-matrix interface is in compression during cooling and tension during heating (Takao and Taya, 1985). Thus as damage evolves, it is probably more appropriate to use $f_{tot} = f_b + f_d$ during the heating portion of the thermal cycle and $f_{tot} = f_b$ during the cooling portion.

4.3 Sample Calculations

To illustrate, numerical computations have been performed using material properties typical of SiC whisker reinforced 6061-T6 Al as given by Morimoto et al. (1988). Unless otherwise noted, the creep thermal cycling parameters used are: $2\tau = 200$ s, $\Delta T = 350$ K, $\sigma^0 = 10$ MPa, α (aspect ratio) = 5, and $f_{tot} = .2$. The material properties used are $E_{Al} = 67.6$ GPa, $\nu_{Al} = .33$, $\alpha_{Al} = 24.7 \times 10^{-6}$ /K, $E_{SiC} = 427$ GPa, $\nu_{SiC} = .17$, $\alpha_{SiC} = 4.3 \times 10^{-6}$ /K, $A_{Al} = 1.26 \times 10^{-16}$ Paⁿ/S, $n_{Al} = 4.88$.

Figure 4.4 shows the predicted creep strain versus time for a total volume fraction of reinforcement, $f_{tot} = .15$, at various levels of debonding, $f_d = .15$. It is seen that even though the matrix is assumed to be in steady-state creep, the composite exhibits a period of transient creep. It is readily apparent that the presence of debonded fibers dramatically affects the creep behavior of the MMC. Also shown in Fig. 4.4 are experimental results for a SiC whisker/6061-T6 Al short fiber composite which fall between the predictions for significant debonding. The analytical prediction for the stress at the fiber-matrix interface at time, $t=0$, is $\sigma_{ib} = 257$ MPa which significantly exceeds the ultimate strength of unreinforced 6061-T6 Al at 573K. It is thus likely that significant debonding existed from the onset which agrees with the predictions of the proposed model. In Fig. 4.5, the capabilities of the present model with regards to the effects of fiber-matrix debonding are illustrated. Fiber-matrix debonding is assumed to be described by the Weibull statistics of eqs. (4.15) and (4.16) where it is assumed that $\sigma_{ib}^0 = 180$ MPa (roughly twice the ultimate strength of 6061-T6Al at 573K) corresponding to a fairly strong bond. The effects of the Weibull shape parameter on the creep strain of the composite are shown in Fig. 4.5 where the corresponding Weibull probability and cumulative density functions are shown in the inset. It is readily seen that the proposed approach allows simulation of the entire creep strain vs. time curve of an aligned short fiber composite with the exception of the creep rupture strain.

In Fig. 4.6, the accumulated strain as a function of the number of thermal cycles is shown for various values of f_d , for a SiC/Al MMC subjected to thermal cycling creep loading. The highly nonlinear response as a function of f_d is clearly evident. The progression of damage appears as a jumping from the bottom line in Fig. 4.6 ($f_d = 0$) up to higher values of f_d with increasing N resulting in an overall nonlinear response of the composite. This is in qualitative agreement with experimental findings of Yoda et al. (1978) and Armstrong et al. (1991) for thermal cycling. The predicted accumulated strain of the composite subjected to creep only at T_H , based on the present theory (eqs. (4.8) - (4.14)) is far less than those under thermal cycling creep loadings, thus cannot be plotted in Fig. 4.6 (it would be almost zero in this scale of Fig. 4.6). It is clear that thermal cycling creep results in accumulated strains far in excess of those from isothermal creep which is consistent with numerous experimental reports. Finally, the effects of progressive damage are illustrated in Fig. 4.7 by employing the statistical description assumed in the previous section for various values of the shape parameter, b , at a guaranteed $\epsilon_{cr} = .01$. The effect of b is to broaden the distribution (as b increases) so that the development of damage after ϵ_{cr} is less abrupt as is

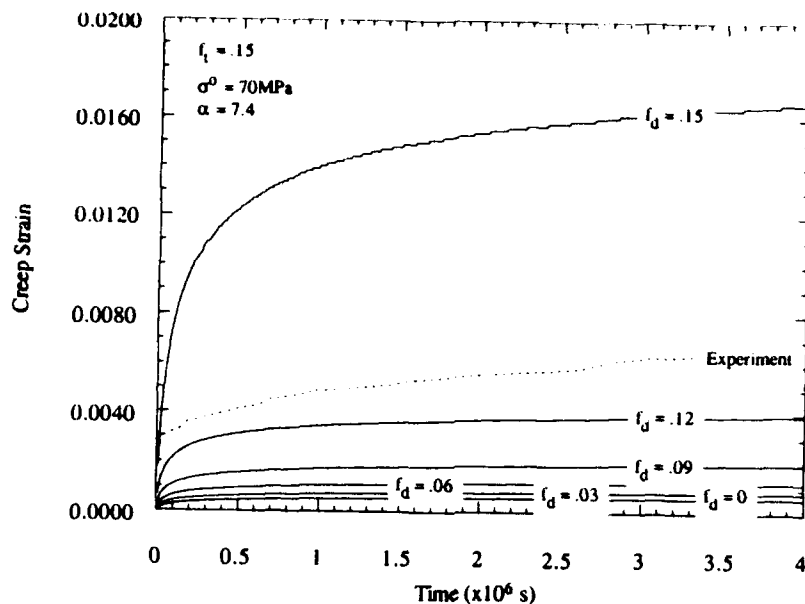


Fig. 4.4 Predicted creep strain-time relation of a SiC whisker/6061 Al matrix composite for various volume fraction of debonded fiber (f_d).

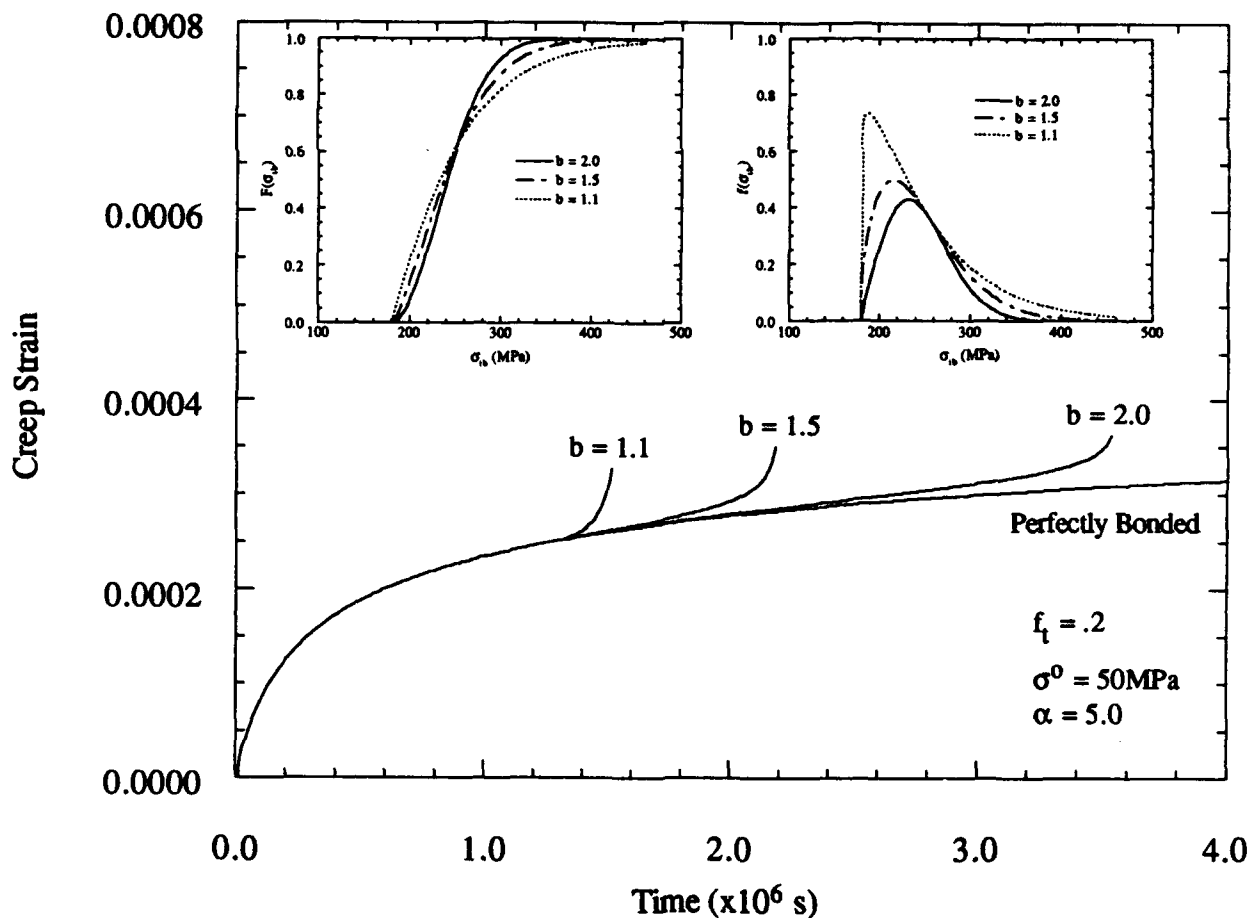


Fig. 4.5 Predicted creep strain-time relation of a SiC whisker/6061 Al matrix composite for various values of shape parameter of Weibull function eq. (4.16).

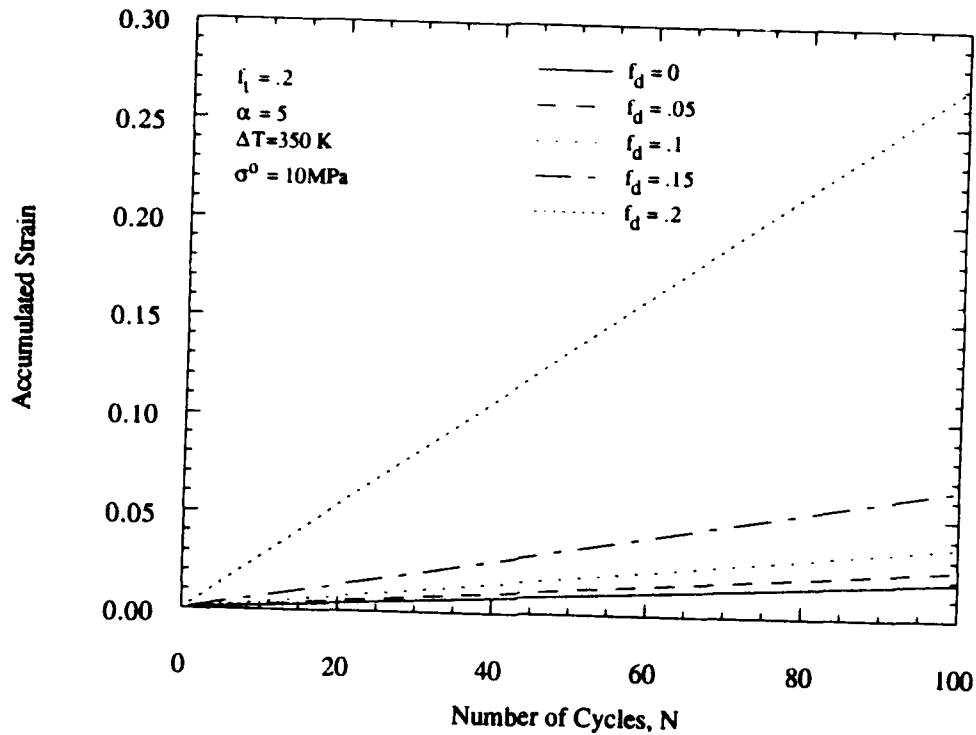


Fig. 4.6 Predicted accumulated strain-thermal cycles relation of a SiC whisker/6061 Al matrix composite subjected to combined creep and thermal cycling.

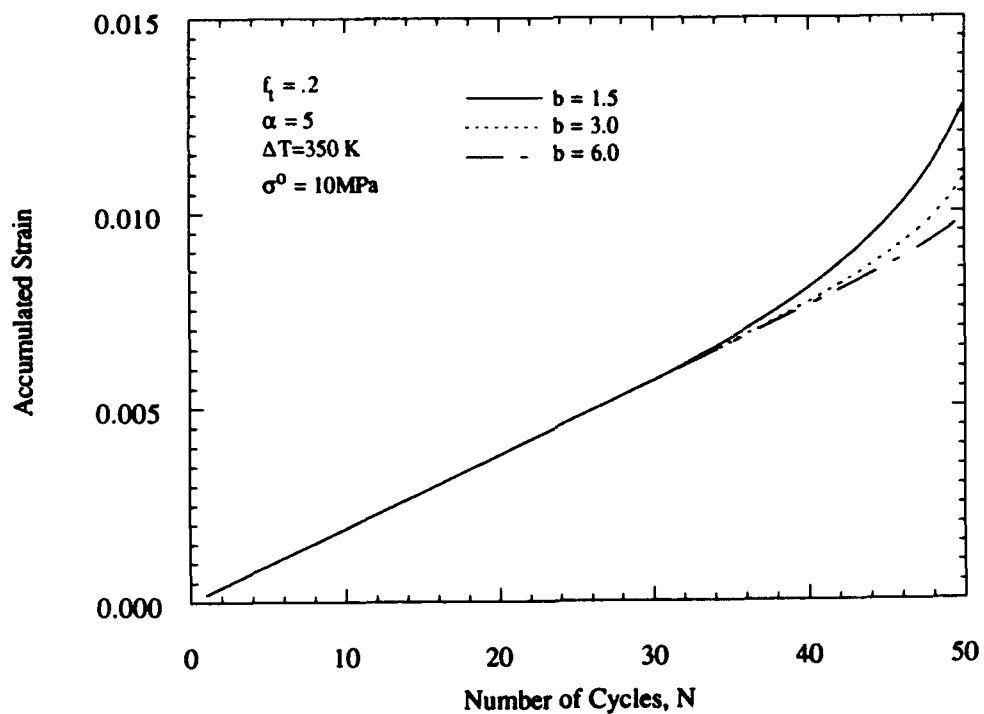


Fig. 4.7 Predicted accumulated strain-thermal cycles relation of a SiC whisker/6061 Al matrix composite subjected to combined creep and thermal cycling for various values of shape parameter b .

evident in Fig. 4.7. Although the example shown in Fig. 4.7 is primarily an illustration of the capabilities of the proposed model, it is evident that the experimentally observed phenomena of increasing nonlinear strain accumulation with progressive damage can be described with this model. Efforts to correlate the interfacial damage with observed strain accumulation are currently underway.

5. Conclusion

Design and assemblage of a new creep thermal cyler with constant stress loading capability were completed. Preliminary data of dimensional change (accumulated axial strain) of SiC particulate/6062 Al matrix composite with $V_f = 10$ and 20% were obtained by using the above creep thermal cyler. The preliminary data support the analytical predictions based on the aligned short fiber metal matrix composite we proposed; the larger the volume fraction of filler, the smaller the dimensional change.

Additional experimental study on measuring the R-curve behavior of Partially Stabilized Zirconia (PSZ) — stainless steel (SS)/PSZ composite — PSZ laminate reveals that the layer of SS/PSZ composite sandwiched in PSZ matrix is effective in increasing the fracture toughness, thus may be usable as a possible crack arrester for otherwise brittle ceramics.

Dislocation punching was identified as a major relaxation mechanism to reduce the interfacial misfit strain induced by the difference in coefficient of thermal expansion. The analytical study covers all the possible interfaces: spherical, 2D curve, ellipsoidal surfaced and planar interfaces. Thus the model proved to be applicable to both metal matrix composite and coated substrate systems. The predicted strengthening due to dislocation punching in as-quenched SiC particle/6061 Al matrix composite agrees well with the experimental observation.

Analytical modeling of creep strain of a metal matrix composite where the interface of some fraction of fibers is debonded, reveals the strong effect of debonded interface on enhancing creep strain, thus weakening of the creep resistance. The effect of interfacial strength is simulated by three-parameter Weibull function, which is then combined with the analytical model for creep thermal cycling. The predicted results of accumulated axial strain (dimensional change) of SiC whisker/Al matrix composite clearly demonstrate the strong effect of the interfacial bond strength on the dimensional change and the importance of the three parameters used in the Weibull function.

6. References

- Armstrong, W. D., Taya, M., and Dunn, M. L., 1991, "Strain Accumulation in Thermal Cycled Metal Matrix Composites," in *Damage and Oxidation Protection in High Temperature Composites*, ASME AD-Vol. 25-2, G. K. Haritos and O. O. Ochoa eds., ASME Winter Annual Meeting, pp. 51-66.
- Armstrong, W.D., and Taya, M., 1991 (July/August), "Design of a new Creep-Thermal Cycler for High-Temperature Metal Matrix Composites", *J. of Experimental Techniques*, p 33-37.
- Ashby, M.F. and Johnson, L., 1969, "On the Generation of Dislocations at Misfitting Particles in a Ductile Matrix," *Phil. Mag.*, Vol. 20, pp. 1009-1022.
- Chawla, K.K. and Metzger, M. 1972, "Initial Dislocation Distribution in Tungsten Fibre-Copper Composites," *J. Mater. Sci.*, Vol. 7, pp. 34-39.
- Chen, Y. and Daehn, G. S., 1991, "The Thermal Cycling Deformation of a Particle Reinforced Metal Matrix Composite: Comparison Between a Model and Experimental Observations," *Scripta Metall.*, Vol. 25, 1543-1548.
- Daehn, G. S. and Gonzalez-Doncel, G., 1989, "Deformation of Whisker-Reinforced Metal-Matrix Composites Under Changing Temperature Conditions," *Metall. Trans.*, Vol. 20A, pp. 2355-2368.
- Derby, B., 1991, in *Proc. of the 12th Riso International Symposium on Materials Science: Metal Matrix Composites - Processing, Microstructure, and Properties*, N. Hansen et al., eds., pp. 149-171.
- Dragone, T. L., Schlautmann, J. J., and Nix, W. D., 1991, "Processing and Creep Characterization of a Model Metal Matrix Composite: Lead Reinforced with Nickle Fibers," *Metallurgical Transactions A*, Vol. 22A, pp. 1029-1036.
- Dunand, D.C. and Mortensen, A., 1991, "On the Relaxation of a Mismatching Spheroid by Prismatic Loop Punching," *Scripta Metall. Mater.*, Vol. 25, pp. 761-766.
- Dunn, M. L. and Taya, M., 1992, "Thermal Cycling Creep of Metal Matrix Composites," *Scripta Metallurgica*, Vol. 27, pp. 1349-1354.
- Echigoya, J., Taya, M., and Armstrong, W. D., 1991, "An Investigation into the Degradation Mode of W-ThO₂/FeCrAlY Metal Matrix Composite Under Thermal Cycling," *Materials Science and Engineering*, Vol. A141, pp. 63-66.
- Eshelby, J. D., 1957, "The Determination of the Elastic Field of an Ellipsoidal Inclusion, and Related Problems," *Proceedings of the Royal Society of London*, Vol. A241, pp. 376-396.
- Garofalo, F. , Richmond, O., and Domis, W.F., 1962, "Design of Apparatus for Constant-Stress or Constant-Load", *J. Basic Eng.*, Vol. 84, p 287-293.
- Freund, L.B., 1987, "The Stability of a Dislocation Threading a Strained Layer on a Substrate," *J. Applied Mech.*, Vol. 54, pp. 553-557.
- Hedyes, S.M. and Mitchell, J.W., 1953, "Observation of Polyhedral Sub-Structure in Crystals of Silver Bromide," *Phil. Mag.*, Vol. 44, pp. 223-224.
- Matthews, J.W. and Blakesee, A.E., 1974, "Defects in Epitaxial Multilayers," *J. Crystal Growth*, Vol. 27, pp. 118-125.
- Mori, T., and Tanaka, K., 1973, "Average Stress in Matrix and Average Elastic Energy of Materials With Misfitting Inclusions," *Acta Metallurgica*, Vol. 21, pp. 571-574.
- Mura, T., 1987, *Micromechanics of Defects in Solids*, Second ed., Martinus Nijhoff Publisher.
- Nieh, T. G., 1984, "Creep Rupture of a Silicon Carbide Reinforced Aluminum Composite," *Metallurgical Transactions A*, Vol. 15A, pp. 139-146.
- Odqvist, F. K. G., 1974, *Mathematical Theory of Creep and Creep Rupture*; Oxford Press.
- Pan, H. H. and Weng, G. J., 1992, "An Energy Approach to the High-Temperature Creep of Fiber-Reinforced Metal-Matrix Composites," in *Damage Mechanics in Composites*, ASME AMD-Vol. 150/AD-Vol. 32, D. H. Allen and D. C. Lagoudas eds., ASME Winter Annual Meeting, pp. 195-212.

- Pandey, A. B., Mishra, R. S., and Mahajan, Y. R., 1993, "Creep Fracture in Al-SiC Metal Matrix Composites," *Journal of Materials Science*, Vol. 28, pp. 2943-2949.
- Povirk, G. L., Nutt, S. R., and Needleman, A., 1992, "Analysis of Creep in Thermally Cycled Al/SiC Composites," *Scripta Metall.*, Vol. 26, pp. 461-466.
- Shibata, S., Mori, T., and Taya, M., 1992, "Stress Relaxation by Dislocation Punching to Radical Direction from a Long Fiber in a Composite," *Scripta Metall. Mater.*, Vol. 26, pp. 363-368.
- Shibata, S., Taya, M., Mori, T., and Mura, T., 1992, "Dislocation Punching from Spherical Inclusion in a Metal Matrix Composite," *Acta Metall. Mater.*, Vol. 40, No. 11, pp 3141-3148.
- Shieu, F.S. and Sass, S.L., 1991, "Dislocation Mechanisms for the Relaxation of Thermal Stress at Metal-Ceramic Interfaces," *Acta Metall. Mater.*, Vol. 39, No. 4, pp. 539-547.
- Shieu, F.S. and Sass, S.L., 1990, "Experimental and Theoretical Studies of the Dislocation Structure of NiO-Pt Interfaces," *Acta Metall. Mater.*, Vol. 38, No. 9, pp. 1653-1667.
- Takao, Y., and Taya, M., 1985, "Thermal Expansion Coefficients and Thermal Stresses in an Aligned Short Fiber Composite With Application to a Short Carbon Fiber/Aluminum," *Journal of Applied Mechanics*, Vol. 107, pp. 806-810.
- Tanaka, K., Narita, K., and Mori, T., 1972, "Work Hardening of Materials with Strong Inclusions After Prismatic Punching," *Acta Metall.*, Vol. 20, p. 297.
- Tanaka, K. and Mori, T., 1970, "The Hardening of Crystals by Non-Deforming Particles and Fibers," *Acta Metall.*, Vol. 18, pp. 931-941.
- Tanaka, K., Mori, T., and Nakamura, T., 1970, "Cavity Formation at the Interface of a Spherical Inclusion in a Plastically Deformed Matrix," *Phil. Mag.*, Vol. 21, pp. 267-279.
- Taya, M., Armstrong, W. D., and Dunn, M. L., 1993, "Thermal Cycling Damage of Metal Matrix Composites," *Applied Mechanics Reviews*, in press.
- Taya, M., Lulay, K.E., and Lloyd, D.J., 1991, "Strengthening of a Particulate Metal Matrix Composite by Quenching," *Acta Metall. Mater.*, Vol. 39, No. 1, pp. 73-87.
- Taya, M., 1991, "Creep Behavior of Metal Matrix Composites," Ch. 6 in *Metal Matrix Composites: Mechanisms and Properties*, eds. R.K. Everette and R.J. Arsenault, Academic Press, pp. 169-187.
- Taya, M., and Arsenault, R.J., 1989, *Metal Matrix Composites, Thermomechanical Behavior*, Pergamon Press.
- Taya, M., and Mori, T., 1987, "Modeling of Dimensional Change in Metal Matrix Composites Subjected to Thermal Cycling," *Thermomechanical Couplings in Solids*, eds. H. D. Bui and Q. S. Nguyen, pp. 147-162.
- Taya, M. and Mori, T., 1987, "Dislocations Punched Out Around a Short Fiber in a Short Fiber Metal Matrix Composite Subjected to Uniform Temperature Change," *Acta Metall.*, Vol. 35, p. 155.
- Taya, M., and Chou, T. W., 1981, "On Two Kinds of Ellipsoidal Inhomogeneities in an Infinite Elastic Body: An Application to a Hybrid Composite," *International Journal of Solids and Structures*, Vol. 17, pp. 553-563.
- Vogelsang, M., Fischer, R.M. and Arsenault, R.J., 1986 "An In situ HVEM Study of Dislocation Generation at Al/SiC Interfaces in Metal Matrix Composites," *Metall. Trans.*, Vol. 17A, pp. 379-389.
- Wang, Y. M. and Weng, G. J., 1992, "Transient Creep Strain of a Fiber-Reinforced Metal-Matrix Composite Under Transverse Loading," *J. Eng. Mat. and Technology*, Vol. 114, pp. 237-244.
- Weng, G. J., 1987, "A Micromechanical Theory of High Temperature Creep," *J. Appl. Mech.*, Vol. 54, pp. 822-827.
- Zhang, H., Daehn, G. S., and Wagoner, R. H., 1991, *Scripta Metall.*, Vol. 25, pp. 2285.

- Zhu, Z. G. and Weng, G. J., 1990a, "Creep Anisotropy of a Metal Matrix Composite Containing Dilute Concentration of Aligned Spheroidal Inclusions," *Mechanics of Materials*, Vol. 9, pp. 93-105.
- Zhu, Z. G. and Weng, G. J., 1990b, "A Local Theory for the Calculation of Overall Creep Strain of Particle-Reinforced Composite," *International Journal of Plasticity*, Vol. 6, pp. 449-469.
- Zhu, Z. G. and Weng, G. J., 1989, "Creep Deformation of Particle-Strengthened Metal Matrix Composites," *J. Eng. Mat. and Technology*, Vol. 111, pp. 99-105.

7. List of Publications During the First Year Period

- (1) Taya, M., Armstrong, W.D. and Dunn, M. 1993, "Thermal Cycling Damage of Metal Matrix Composites: Analytical Study on Dimensional Change," *Applied Mech. Review*, vol. 46 No. 5, pp. 1-10.
- (2) Dunn, M. and Taya, M. 1992, "Thermal Cycling Creep of Short Fiber Metal Matrix Composites," *Scripta Metall. Mater.*, Vol. 27, pp. 1349-1354.
- (3) Dunn, M.L. and Taya, M., 1993, "Modeling of Thermal Cycling of Damaging Short Fiber Metal Matrix Composites," *Mater. Sci. Eng. -A*, in press.
- (4) Dunn, M. and Taya, M. 1993, "Creep And Thermal Cycling Creep of Metal Matrix Composites," to appear in ASME Bound Volume on *Thermomechanical Behavior of Advanced Structural Materials*, ed. W.F. Jones.
- (5) Taya, M. and Mori, T. 1993, "Dislocation Punching from Ceramic-Metal Interfaces," under review for *J. Eng. Mater. Tech.*
- (6) Liu, M.S., Taya, M. and Armstrong, W.D. "Creep and Thermal Cycling Fixture Design for Metal Matrix Composites," submitted to *Experimental Mechanics*.
- (7) Li, Z., Taya, M., Dunn, M.L. and Watanabe, R. "Fracture Toughness of PSZ-SS/PSZ Composite-PSZ Laminate," submitted to *J. Am. Cer. Soc.*